TOWARDS SCALABLE SYNTHESIS METHODS FOR NICKEL–MOLYBDENUM ALKALINE HYDROGEN EVOLUTION CATALYSTS

by

Aayush Mantri

BE Chemical Engineering, Manipal University, 2014

Submitted to the Graduate Faculty of

the Swanson School of Engineering in partial fulfillment

of the requirements for the degree of

Master of Science

University of Pittsburgh

2018

UNIVERSITY OF PITTSBURGH

SWANSON SCHOOL OF ENGINEERING

This thesis was presented

by

Aayush Mantri

It was defended on

March 28, 2018

and approved by

James McKone, Ph.D., Assistant Professor,
Department of Chemical and Petroleum Engineering

Götz Veser, Ph.D., Professor,
Department of Chemical and Petroleum Engineering

Susan Fullerton, Ph.D., Assistant Professor,
Department of Chemical and Petroleum Engineering

Thesis Advisor: James McKone, Ph.D., Assistant Professor,
Department of Chemical and Petroleum Engineering

TOWARDS SCALABLE SYNTHESIS METHODS FOR NICKEL–MOLYBDENUM ALKALINE HYDROGEN EVOLUTION CATALYSTS

Aayush Mantri, M.S.

University of Pittsburgh, 2018

Hydrogen is a critical chemical reagent, important as a chemical feedstock and as an energy carrier for the future. However, a majority of it is produced from unsustainable fossil fuel sources while the existing electrochemical routes for H_2 generation that can replace these conventional sources continue to remain economically uncompetitive. Alkaline Electrolyzers offer a well matured, comparatively low-cost electrolysis technology for sustainable H_2 production. An important barrier towards the success of this technology is the identification of efficient, inexpensive, stable non-precious material for catalyzing the hydrogen evolution reaction in these systems. Nickel –Molybdenum (Ni–Mo) catalysts have been recognized as a promising candidate to overcome this barrier.

This work focuses on developing an efficient and scalable route for synthesizing Ni–Mo nanopowders while limiting the toxicity profile of the synthetic methods identified previously It also delves into the evaluation of the structure-function-activity relationships demonstrated by these systems; testing the feasibility of some common strategies for enhancement of their catalytic activities based on the prior study. In particular, we found that the addition of carbon additives alleviates conductivity issues present in these systems, resulting in a significant enhancement in the electrochemical performance of these catalysts.

An overarching goal behind the entirety of this work has been to identify the most active Ni–Mo based systems that can be synthesized in a scalable and sustainable manner and are readily usable in modern–day electrolyzer installations.

TABLE OF CONTENTS

LIST OF TABLES

LIST OF FIGURES

PREFACE

Graduate school has been a challenging but fulfilling experience through which I have sought the support of many wonderful mentors, colleagues, friends, and family members without which it would not have been possible to complete this dissertation.

I would like to begin by thanking my advisor, Dr.James R. McKone who has been a mentor to me in every sense of the word during my time here at Pitt. The advice and guidance he has provided have been critical in shaping not only research work but also my approach and thought process towards science in general. I have benefited greatly from his remarkable depth of knowledge and his extreme willingness to share insights on topics within and beyond the academic domain. I will be ever grateful for the deep commitment he has shown towards my professional development along with the encouragement and support he has shown in helping me pursue all relevant opportunities while I was here. As one of the first students graduating from his research group, I hope I do him proud.

I would also like to thank the other members of my dissertation committee - Dr.Götz Veser and Dr.Susan Fullerton for helping critique my work. It will help me keep true to the work as I try to meet the high expectations they maintain. Along with them, I thank all the other faculty and staff members at Pitt who have directly or indirectly supported and advised me during my time here.

I have had the good fortune to work with some extremely talented colleagues while associated with the McKone group. I am particularly thankful to Rituja Patil and Tejal Sawant who have been there to provide help, advice, and feedback since the very start of my work. I would also like to acknowledge Dean Miller, Emily Siegel, Stephen House and Yahui Yang as well as all the staff at the NFCF, each of whom has supported me during many of the studies included in this thesis. The free exchange of ideas that I have been able

to maintain with all of them has been one of the greatest sources for learning for me as a graduate student.

Finally, I would like to extend gratitude towards my family and friends. My parents, Naresh and Alka Mantri who have brought me up with the greatest love and care, pressed me to be my best and paved my way through life. My siblings - Aastha who has always been there to set an example for me as well as Gaurav, Ruchi , and Varun who have always been there for me. Also my friends, Sukrit, Daksh, Raj, Sakshi, Kedar, Sateendra, Aditya, Gaurav, Peter and Malik for helping me keep touch with the lighter moments of life, letting me maintain a balance during a rather demanding two years of graduate school. Thanks at last to Palak Narang, who has been a constant source of comfort, for her love and patience through the many highs and lows of my time here.

1.0 INTRODUCTION

1.1 PURPOSE AND SCOPE

The following thesis presents in detail the entirety of the work that I have pursued over the course of my involvement with the McKone group. It has been written in part to satisfy the requirements for a masters degree in chemical engineering from the University of Pittsburgh.

The remainder of Chapter-1 presents a general overview of the field of electrochemical hydrogen production based on the understanding I have developed during the course of this work. It focuses primarily on alkaline hydrogen evolution systems which are the target configuration for these systems along with a brief introduction on catalyzing these reactions.

The thesis continues in Chapter-2 with a thorough description of our work with Ni–Mo composite HER catalysts meant for alkaline electrolysis. It presents the development of a fresh synthetic scheme for producing unsupported Ni–Mo nanopowder catalysts along with the experimental techniques and results form the physical and electrochemical characterization studies done on them.

Chapter-3 provides our evaluation of the structure-function-activity relationships in the as-synthesized Ni–Mo catalysts. It will cover the significance of some of the important process parameters along with our efforts to scale the activity and processability of these catalysts.

The next chapter, Chapter-4, will present the experimental and material synthetic techniques that were learned and employed during the course of this work. This is provided to allow for a better interpretation of the results presented before and to aid any possible reproduction of the following work.

Finally, Chapter-5 will be a summary of my work along with my suggestions towards the potential directions for future work.

I hope that this work will help enhance our understanding of Ni–Mo HER catalysts systems and of alkaline HER catalysis in general and open sufficient avenues for further work on these systems that might extend to meeting our long-term goal of designing practical alkaline electrolyzer systems.

1.2 GLOBAL ENERGY SCENARIO

Energy is the lifeblood of human existence.[1] The availability of an affordable and secure source of energy is necessary for our continued technological and economic prosperity. While global population has expanded essentially linearly over the past several decades, our energy consumption has expanded at exponential rates. Moreover, the source of our energy has changed drastically over the years, as shown in Fig1.[1]

Until the industrial revolution began at the turn of the 19$^{\text{th}}$ century, we relied exclusively on biofuels like wood along with minor contributions from kinetic energies harvested via wind and water.[5] The growth of the industrial sector and automobile industry then drove a rapid transition towards the use of fossil fuels, which continue to dominate the global energy landscape.[6] In recent years energy sources have become more diverse, incorporating hydro, wind, solar bio-fuels and nuclear-based power. Deployment of these newer energy sources has often been driven by either an unequal geo-political access to the more conventional resources across different regions and economic sectors around the globe or national policies aimed at decarbonizing the energy supply.[7,8]

The scale of consumption of inherently exhaustible fossil fuels has raised concerns regarding their continued availability. Moreover, mining and burning fossil fuels also have significant deleterious repercussions on other aspects of human life. There is widespread concern regarding the impact of these fuels on climate, air quality, public health, economic competitiveness, and even geo-political stability.[1 9–11] These concerns are arguably all the more acute in developing countries like China and India, which experience considerable energy stress due to their large and dense populations. These countries expect to see the largest growth in energy consumptions in the coming years due to their rapidly expanding

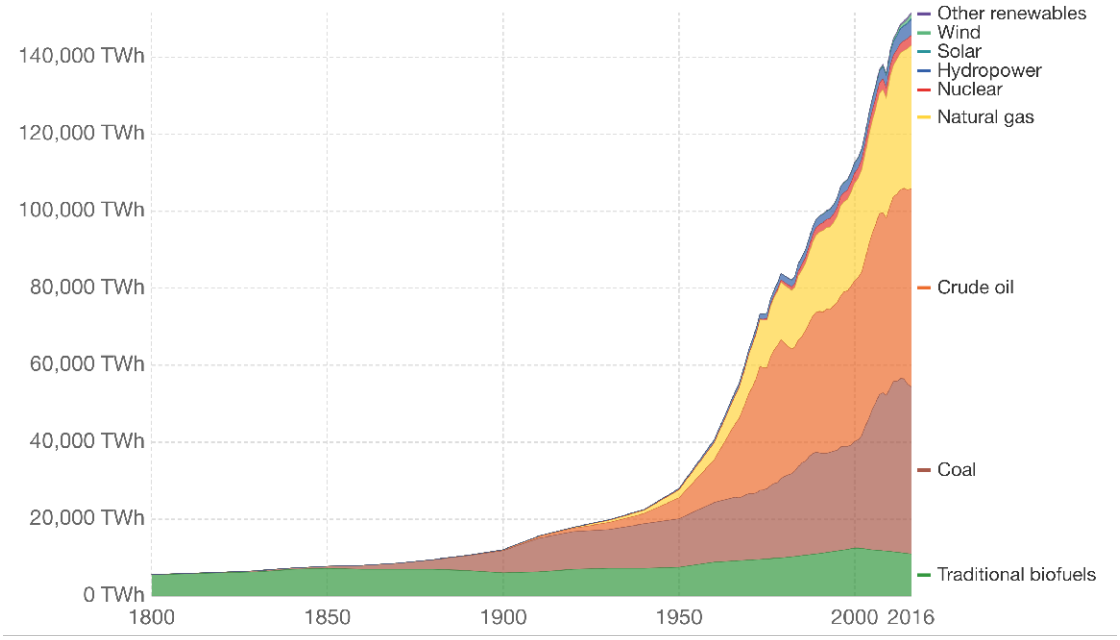

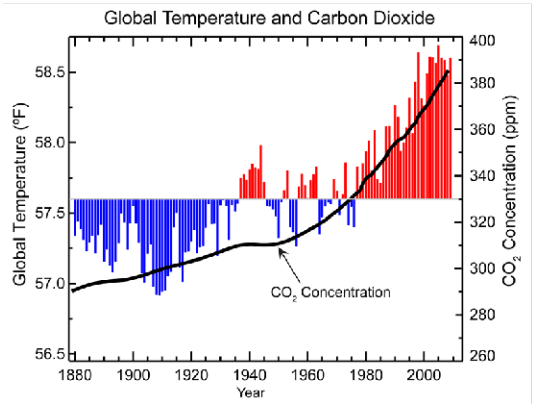

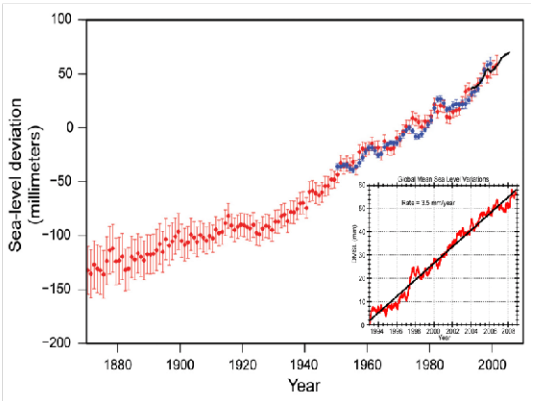

Figure 1: *(a) Plot of total global energy consumption and relative change by the source from 1800 to 2016. (b) Plot of rising global temperatures and CO_2 concentrations from 1880 to 2015 (c) Plot of sea level deviation from the year 1870 to 2010 (inset: Global mean sea level variation from 1993 to 2010)*[2–4]

infrastructure and industrial sectors. However, a bulk of their energy production is still deeply rooted in the conventional sector, given the large fossil reserves in these countries and limited prior investments into the renewable energy sectors.[12,13]

There exists a significant amount of research that convincingly links the growth of fossil fuel consumption to rising rates of pollution—including nitrogen and sulfur oxides and particulates—as well as green house gases (GHGs).[3,14] Some of the harmful effects of these anthropogenic emissions are evident from environmental phenomena like global warming, melting glaciers, and rising sea levels as illustrated in Fig1.

In response to these concerns, 195 countries signed the 2015 Paris agreement to cut emissions with the intention of limiting global warming to well below 2°C above the pre–industrial level.[11] However, given their ubiquitous nature, it is untenable to expect these ambitious goals to be met by lowering the energy consumptions around the world. In fact, the global energy consumption is predicted to rise from 17 TW in 2010 to 27 TW by 2040.[15] This makes the need to transition away from these carbon-based resources towards cleaner, sustainable sources of energy like solar, wind and bio–fuels all the more imperative.

It has been argued that a significant proportion of the anticipated global energy demands can be feasibly offset by each of the various renewable energy resources that are already available.[9] The Intergovernmental Panel on Climate Change (IPCC) has even claimed that technologies that exist in operation or pilot stage today are sufficient to follow a less–than doubling trajectory over the next hundred years or more.[16,17] However, it would be an oversight to ignore the significant techno–economic challenges that do exist for this to happen.

A key limitation that has hindered widespread implementation of renewable energy sources is the inherent intermittence in their supply.[10] Chemical energy storage is seen as a promising approach to buffer against such temporal changes in energy supply to support the transition to renewable energy sources. Hydrogen has been touted as a prime candidate for such energy storage applications, due to its abundance, high energy density and carbon neutral oxidation.[6,18,19] This has resulted in an aggressive research into identifying sustainable hydrogen production technologies that can help support the transition from fossil fuels to renewable energies.

1.3 HYDROGEN

Hydrogen is already an important chemical reagent since it is a critical feedstock for a host of industrial processes.[6,20] Moreover, the high energy density and low environmental impact of H_2 has inspired projections of a "hydrogen economy" over the years, where H_2 is proposed as both a transportation fuel and electric grid storage material.[19,21–25] Unfortunately, a significant amount of this H_2 is currently sourced from fossil fuel based production routes, primarily via industrial steam reforming or coal gasification.By comparison, hydrogen production via water electrolysis accounts for only 4% of the global hydrogen production market.[26] Although conventional steam reforming and coal gasification are low energy efficiency conversion processes that yield low purity H_2, their extensive use is driven by the comparatively low cost of the feedstock—natural gas and coal—used in each respective process. The abundance of water resources and high purity of H_2 yield from electrolysis represents an effective and sustainable alternative for hydrogen production, limited primarily by the comparatively higher capital costs associated with it. The DOE has set a target of \$2/kg-H_2 for economical viability of the electrolysis based technology. As of 2009, an independent review by the DOE estimated this cost of hydrogen generation from a central electrolysis operation was estimated anywhere between \$2.70-3.50/kg-H_2; evaluated at an assumed renewable-based electricity cost of \$0.045/kWh.[27]

It is important to note that even beyond its potential applications towards the future energy infrastructure, H_2 already supports a number of heavy volume industries with a global annual consumption estimated at 55 million tonnes.[26] The fertilizer industry uses H_2 to react with N_2 for NH_3 production via the Haber-Bosch process. H_2 also supports the petroleum refining industry, used for hydrogenation and hydrodesulferization of crude to produce diesel and gasoline along with other hydrocarbon-based products.[20,28] At current production levels this already represents \$100 bn. market size, a significant economic incentive to develop cost-effective water electrolysis technologies.[18,29]

1.4 WATER ELECTROLYSIS AND ALKALINE ELECTROLYZERS

Water electrolysis is based on the principle of using electrical energy as a driving force to split water into hydrogen and oxygen. This phenomenon has been known for over 200 years, with the first recorded observations coming as early as 1789.[30] It was subsequently developed by Nicholson and Carlisle in the 1800s and by the 1900s, we already had commercially operating electrolyzer systems operating on this principle.[31]

The overall water electrolysis reaction is as follows:

$$2\,H_2O(l) \longrightarrow 2\,H_2(g) + O_2(g) \tag{1.1}$$

The thermodynamic energy requirement for this process is $\Delta G = 237.1$ kJ/mol under standard conditions. The cell voltage corresponding to this requirement as given by the Nernst equation amounts to 1.23 V.[32,33] This redox reaction takes place in the form of two spatially separated half-reactions in the presence of an electrolyte: the hydrogen evolution (HER) at the cathode and the oxygen evolution (OER) at the anode.[34]

$$\text{HER:} \quad 4\,H^+ + 4\,e^- \longrightarrow 2\,H_2 \tag{1.2}$$

$$\text{OER:} \quad 2\,H_2O + O_2 \longrightarrow 4\,H^+ + 4\,e^- \tag{1.3}$$

In practice, however, the reaction tends to require potentials in excess of the thermodynamic requirement, due to the presence of kinetic and transport limitations inherent in the system. This excess potential is commonly known as overpotential, η. The practical operating potential for effecting water splitting is, therefore, more often described as:[35]

$$E_{op} = 1.23V + \eta_a + \eta_c + \eta_{other} \tag{1.4}$$

The resistances associated with the electrochemical cell construction and electrolytes, such as solution resistance and contact resistances account for the η_{other} in equation1.4 while the η_a and cathode η_c correspond to the activation barriers present on the anode and cathode respectively.

The reduction of these overpotentials is the key to making water electrolysis more energy efficient. This is done by improving the cell construction and choice of electrolytes within

the system and by effectively catalyzing the anode and cathode reaction. These goals form the basis for much of the research associated with these systems. A schematic of a typical water electrolyzer system is shown in Fig 2.

As mentioned above, electrolyzer systems are a mature technology that have found modest use in industrial hydrogen production for almost a century.[26] At present, these systems are popular under three major configurations: the alkaline electrolyzer, the polymer electrolyte membrane (PEM) electrolyzer, and the solid oxide electrolyzer.[36] The earliest electrolyzers were Ni-based alkaline electrolyzer systems. These electrolyzer had low capital intensity, owing to the use of earth-abundant catalysts as well as low-cost electrolyte and structure materials, which made them popular options for low capacity hydrogen production, especially to support ammonia production facilities during the early 1900s.[36–39] The commercialization of perfluorinated sulfonic acid membrane materials, most notably Dupont's Nafion in the 1960s, triggered a transition to noble metal-based polymer exchange membrane electrolyzers (popularized by General Electric).[39–42] The high current densities derived from these systems made PEM electrolyzers the industry standard, especially for high purity hydrogen production. However, commercial PEM systems are limited to use in small hydrogen and oxygen production capacities due to high material costs and a limited overall lifetime. Solid Oxide Electrolyzer Cells (SOEC) have seen comparatively lower success due to is high operating temperatures and consequent material challenges.[36]

A rapidly evolving conceptual development to integrate water electrolysis with other renewables for energy storage applications has triggered a broad reevaluation of these technologies in research labs and early-stage commercialization efforts. Both PEM and Alkaline Electrolyzer have been commercially prevalent technologies.[43] Traditionally, PEM electrolyzers have targeted the smaller capacities, and alkaline systems have dominated the high-capacity industrial market.[?] PEM systems offer the advantage of operation at high current densities, variable partial load, overload, and flexible on/off conditions and production of pressurized hydrogen that is suitable for energy transportation use as well as compact plant designs, but their scalability is limited due to the use of costly noble metal catalysts.[27,43] The use of acid electrolytes in the system also broadly prohibits the use of earth-abundant catalysts, especially for anodes, that would otherwise bring the price down. On the other

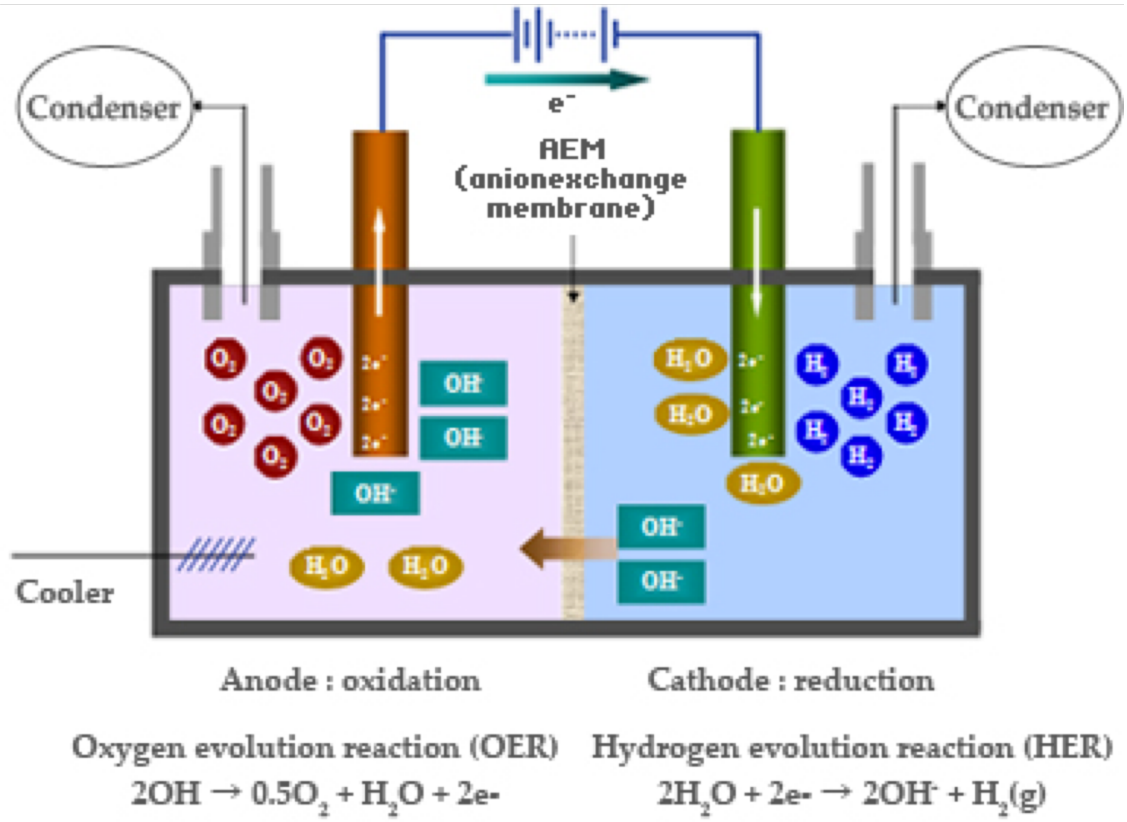

Figure 2: *Schematic of a typical water electrolyser system*

hand, alkaline electrolyzers are based on earth-abundant catalysts that are viable for scale up and additionally offer longer life times. In theory, these systems could potentially offer similar efficiencies to existent PEM systems, provided the associated electrocatalysts and membranes are able to attain a suitable level of maturity for commercial use. A number of the advantages associated with PEM systems are enabled by the use of good ion-exchange membranes. Hence, researchers like those with GEs Advanced Alkaline Electrolysis program have been trying to develop state-of-the-art MEA assemblies for alkaline systems that may enhance the activity of alkaline electrolyzers significantly.[27,44]

The viability of this electrolyzer system for grid applications for energy storage or transportation is strongly dependent on the ability of these systems to provide a high H_2 production capacity at cost parity with existing fossil-based H_2 production technologies. In view of this, alkaline electrolyzer systems represent a well matured, comparatively low-cost technology that can be appropriately enhanced to meet these requirements, hence forming the overarching target configurations for this work.[36]

1.5 CATALYZING THE HYDROGEN EVOLUTION REACTION

Water splitting is known to exhibit sluggish HER and OER kinetics in the absence of suitable catalysts, often needing potentials well in excess of the thermodynamic requirements for these reactions. Therefore, suitable catalysts are used to enhance the reaction kinetics in order to make the system more efficient. The identification of suitable electrocatalysts are a critical step to implementation of an efficient, robust, and commercially viable electrolysis system.

It is important that these catalysts are active towards their respective reactions and also maintain stability over commercially relevant time scales. At present, state-of-the-art HER and OER catalysts systems are often made up of noble metals.[45–51] However, notable recent successes have been achieved in identifying earth-abundant catalysts for alkaline oxygen evolution. Mixed Ni–Fe oxides have been shown to exhibit catalytic activity in base that compares well to Ru/Ir oxides operating in acid.[52,53] Benchmarking studies have also shown that $NiCoO_x$ along with $NiFeO_x$ as reasonably active OER catalysts in alkaline systems.[45]

In this work, however, we will focus on the electrocatalysts for catalyzing the HER. It happens to be one of the most well-studied electrochemical reactions and is thought to proceed via one of two possible mechanisms depending on the catalyst surface: either the Volmer-Tafel or a Volmer-Heyrovsky mechanism.[54] For alkaline systems, these reactions can be represented as[55]

$$\text{Volmer:} \quad H_2O + e^- \longrightarrow H_{ad} + OH^- \tag{1.5}$$

$$\text{Tafel:} \quad H_{ad} + H_{ad} \longrightarrow H_2 \tag{1.6}$$

$$\text{Heyrovsky:} \quad H_2O + H_{ad} + e^- \longrightarrow H_2 + OH^- \tag{1.7}$$

The mechanism in either case is known to involve the interaction between the surface and bound hydride intermediates. Hence, the activity of the catalyst is strongly dependent on the free energy of H_2 adsorption, ΔG_H on the catalyst surface. If the H_2 to surface bond is too weak, the adsorption step will limit the overall reaction rate. If the H_2 to surface bond is too strong, the reaction-desorption step will limit the overall reaction rate. This relationship is explained by the Sabatier principle, which states that the interaction between the catalysts and substrate should be intermediate to allow facile binding of reactant as well as release of product.[56,57] This principle is encapsulated in peaked curves widely known as volcano plots, which relate catalytic activities to ΔG_H as illustrated in Fig 3.[58,59]

As expected, the noble exhibit intermediate M–H bond strengths and therefore occupy the peak position on volcano plots for the HER in both acid and base. Such plots have been a guiding principle for identifying potentially suitable catalyst systems such as MoS_x.[61–63] It should however be noted that for alkaline systems, the observed catalytic activity may also depend strongly on the dynamics and energetics of water and hydroxide species on or near the catalyst surface.[64,65] This complicates the validity of the associated volcano plot and may explain why even Pt catalyst are much less active toward the HER in base as compared to acid conditions.[66]

A large number of HER catalysts have been proposed over the years, showing varying degrees of hydrogen evolution activity and stability in alkaline systems. Among these, nanostructured Pt continues to display the highest inherent activity towards the HER.[51,67,68]

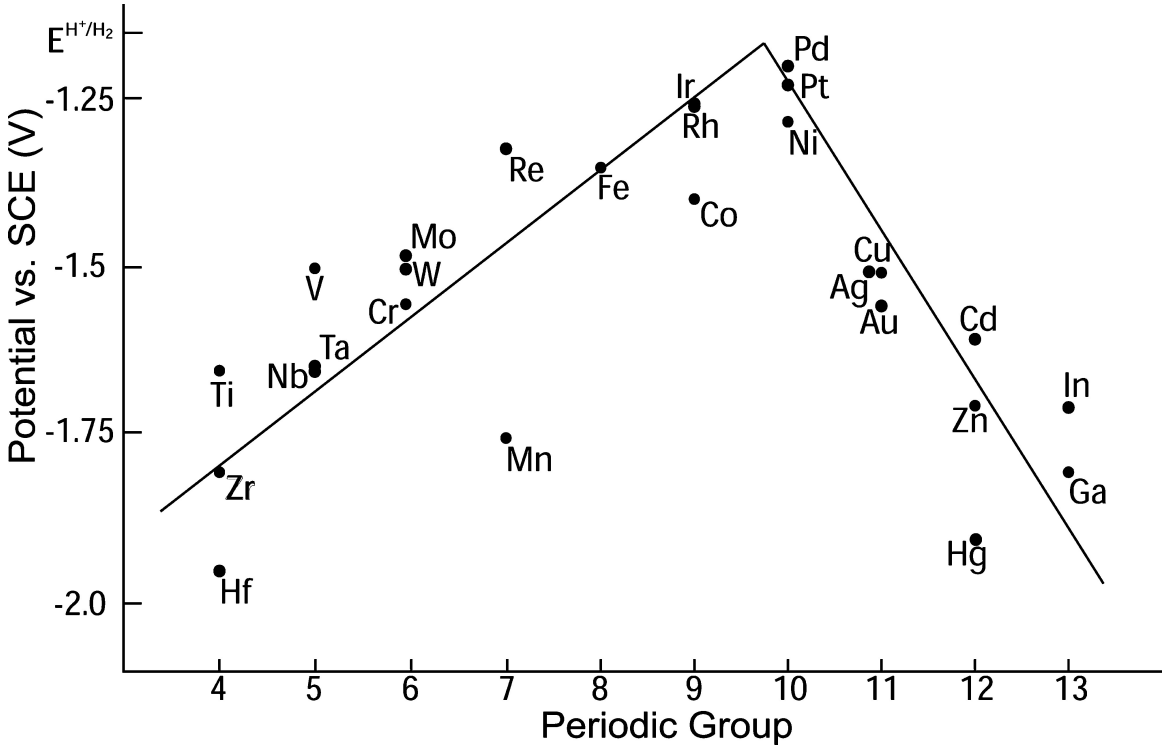

Figure 3: *Volcano plots for the HER base solutions, from Walter et al. Activities in base are correlated to periodic group, which is a rough proxy for M–H bond strength.*[60]

Nevertheless, there are a range of earth-abundant catalysts that have shown promise as potential replacements to Pt.[46,66] These primarily arise out of two class of materials. The first class is transition metal composites along with their oxide/hydroxides, like the Ni/NiOH systems developed by Markovic et al. and the analogous $Ni/NiO/Cr_2O_3$ composite systems.[69] Another important example in this class is nanopowder Ni–Mo alloys including those developed by McKone et al. and $MoNi_{4/}MoO_2$ catalyst developed by Zhang.[70,71] It is quite possible that these systems all exhibit the same predominant reaction mechanism wherein interfacial oxides enhance the sluggish water dissociation kinetics to drive the HER. The second large class of earth-abundant HER catalysts are those incorporating heteroatoms like P, S, C, or N.[6,61] In this class, nickel phosphides and molybdenum sulfides are some of the best performing HER systems reported.[61,72] It is clear from the above list that many of the best HER catalysts are based on Ni and its composites. We are pursuing one such class of material namely Ni–Mo alloys. These systems have been known to exhibit high HER activity and excellent stability in base for decades.[73–76] In a recent benchmarking study, McCrory et al. (shown in Fig 4) validated previous reports suggesting Ni–Mo based alloys offer the highest mass-specific activities for HER among many earth-abundant HER systems for use in alkaline media.[46]

However, Ni–Mo HER catalysts still lag behind the benchmark Pt systems used in PEM electrolyzers. Also, the reaction mechanisms responsible for improved activity of Ni–Mo composites over their Ni and Mo constituents alone remains unclear. Hence, these materials are excellent candidates for further study. Moreover, in view of eventual use of these catalysts in commercial electrolyzers, it is important to evaluate the processability and scalability of these catalyst systems. This latter concern represents the over-arching emphasis of the work presented here.

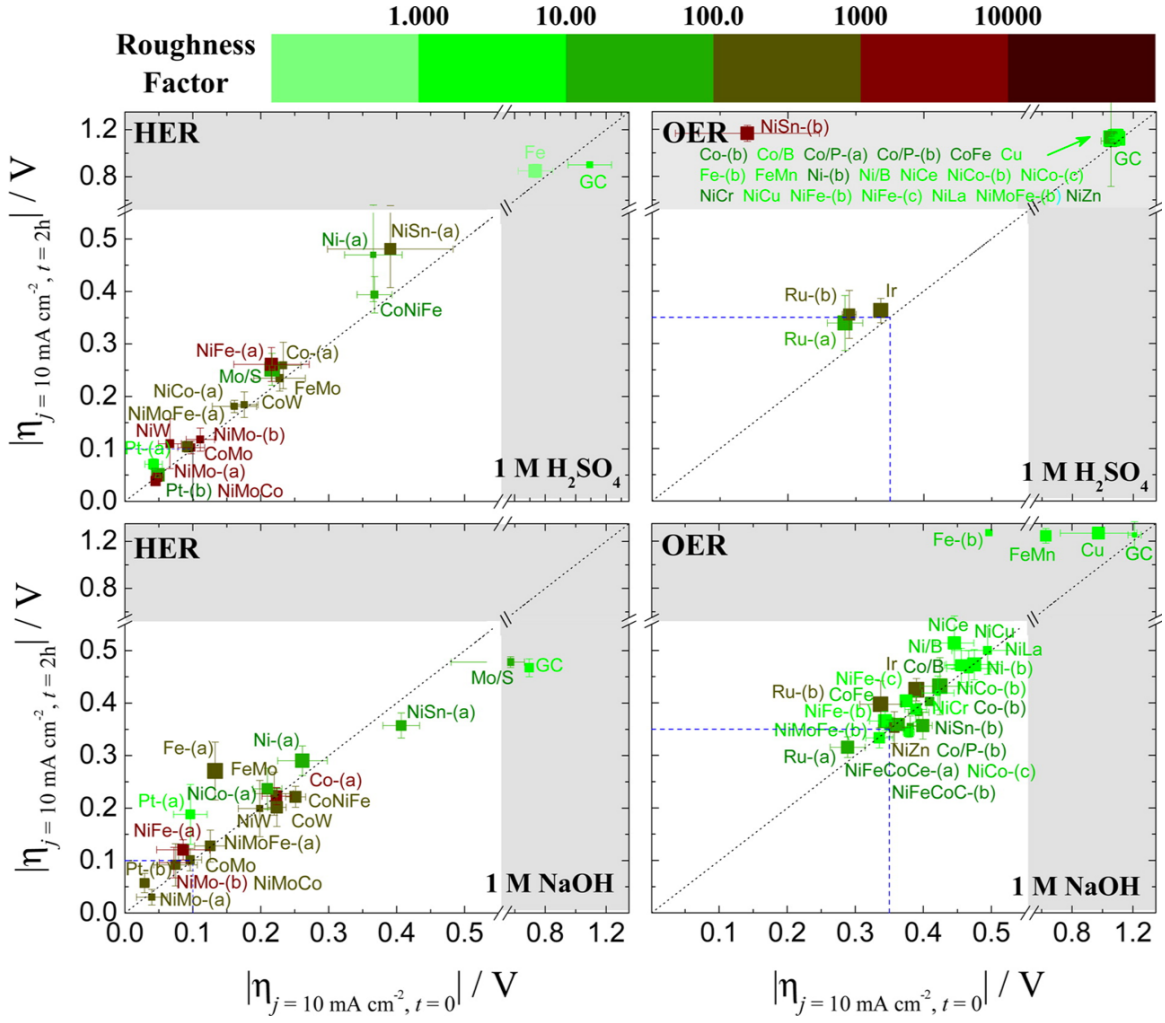

Figure 4: *Plots of catalytic activity, stability, and electrochemically active surface area for HER (left) and OER (right) electrocatalysts in acidic (top) and alkaline (bottom) solutions. The x-axis is the overpotential required to achieve 10 mA/cm^2 per geometric area at time t = 0. The y-axis is the overpotential required to achieve 10 mA/cm^2 per geometric area at time t = 2 h. The diagonal dashed line is the expected response for a stable catalyst that does not change in activity during 2h constant polarization. The color of each point represents the roughness factor of the catalyst with a bin size of 1 order of magnitude with light green representing RF = 1, and dark red representing RF > 104. The size of each point is inversely proportional to the standard deviation in the ECSA measurements. The region of interest for benchmarking is the unshaded white region of the plot where the overpotential required to achieve 10 mA/cm^2 per geometric area at time t = 0 and t = 2 h is less than 0.55 V. There is a break and change in scale in both axes at overpotentials >0.55 V, and the corresponding region of the plot is shown in gray. Catalysts whose activity and stability measurements fall inside this gray area are outside the region of interest for benchmarking, but their activity and stability measurements are included for completeness. The blue boxed regions are the target regions for HER and OER catalysis under the given conditions.Reprinted with permission from (McCrory et al. J. Am. Chem. Soc. 137, 13, 4347-4357). Copyright (2015) American Chemical Society.*[46]

2.0 "AMMONIA-FREE" SYNTHESIS OF NICKEL–MOLYBDENUM HYDROGEN EVOLUTION ELECTROCATALYSTS

This chapter describes work on the synthesis and characterization of the Ni–Mo nanopowder catalyst for HER. It first provides the detailed description of a chemical synthesis developed in the lab that eliminates the ammonia byproduct from the prior synthesis of these catalysts as developed by McKone et al.[70] Subsequently, we ran structural and electrochemical characterization studies on the intermediate and final catalyst phases identifying the prevalent the composition and morphologies of both phases and the HER activity of the final catalyst phase. The catalysts so developed offered high catalytic activities towards HER, comparable to those derived from the original synthesis. We also tried to advance some discussion on identifying the active catalytic sites based on the Transmission Electron Microscopy (TEM) and Energy Dispersive Spectroscopy (EDS) analysis. During the course of this work, I collaborated closely with Rituja Patil who focused on further developing the original Ni-Mo nanopowder synthesis proposed by McKone et al. I was also supported by Dr.Stephen House from Judith Yang's group in order to run TEM analysis on the catalysts and Yahui Yang of Dr.Veser's group to help run UV–Vis experiments.

2.1 INTRODUCTION

As noted in Ch-1, there is a significant potential in alkaline electrochemical H_2 production technologies, whether to support the decarbonization of existing H_2 employing industries or as a means to produce a sustainable mode for energy storage and transportation in the future. In order to realize an effective and commercially viable form of this technology, it is

of prime importance to identify catalysts that are not only effective in catalyzing the reaction but can be sourced and processed in abundance. This is important given the potential scale of the requirement for these systems in the future.

Ni–Mo composite systems have already been reported as one of the most effective earth-abundant HER catalysts systems in base.[46] These systems have been reportedly synthesized both, via electrodeposition techniques as well as chemical synthesis approaches in the past.[70,71,74,76,77] A large majority of this work has come in the form of electrodeposition techniques starting with Conway and then Raj et al. who used electrodeposition of Ni–Mo from aqueous Ni^{2+} and MoO_4^{2-} precursors, highlighting the high geometric activities derived from Ni–Mo and Ni–Mo–Cd amongst other transition metal catalysts.[76,78–82] However it has been the pyrolysis/reduction chemical synthetic approach developed by Brown et al. in their work on transition metal electrodes, and particularly Ni–Mo alloy electrodes that remain one of the highest reported activities for these systems ($>1 A/cm^{-2}$ geometric current density at <100mV overpotential).[73,74,83] These works while significant in yielding interest for these systems, were limited by the fact that they offered either limited control over the mass loadings and/or need direct deposition on substrates and hence lacked flexibility regarding the choice of these substrates. Although these systems were commercially employed in the past, they would offer viability in modern commercial systems since electrocatalysts these days are generally synthesized as unsupported powders or as colloidal inks that can be deposited on any substrate at desired loadings.[70,84,85]

These limitations were largely overcome by McKone et al. who developed a chemical synthetic approach (illustrated in Fig5) adapted from the British Petroleum synthesis and the already known polyol based synthetic techniques to make unsupported Ni-Mo nanopowder alloys during their work on silicon-based hydrogen evolving photocathodes.[9,70] Independent benchmarking studies by McCrory et al.(mentioned earlier in Ch-1) later highlighted these catalysts as one of the highest performing HER catalysts in base.[46] Hence, this synthetic approach became the primary basis for our work. However, it was noted that the presence of an NH_3 by-product in the synthesis raised its toxicity profile and may prove a limitation towards our long-term goal of scalable synthesis of this material.

In the same work, McKone et al. also reported a monotonic increase in activities obtained from metallurgically prepared Ni–Mo alloys with increasing Mo content.[70] However, at the time it was unclear whether the high activity could be attributed to either the alloy or the bulk Mo content. This was further pursued by Csernica and McKone in a recent study on HER activity of the inter-metallic compound Mo_7Ni_7 prepared by thermal reduction of an ammonium nickel molybdate, $NH_4HNi_2(OH)_2(MoO_4)_2$ at 1050°C. They reported an ambiguity in the results regarding the effect of Mo content on activity due to the high degree of sintering and thus a reduction in surface area. However, they did note that upon normalization of activity to the BET surface area, the Mo_7Ni_7 exhibited a 4-fold higher HER activity than the $Ni_{0.92}Mo_{0.08}$ alloy.[86]

These results suggest that an increase in Mo mole fraction within the Ni–Mo catalyst system and/or some combination of crystallographic order with higher bulk Mo might help scale intrinsic HER activity of these Ni–Mo systems and hence served as strong motivation for further study. It was hypothesized that thermally reduced Ni–Mo oxides with a stoichiometric Ni/Mo ratio near unity might help attain alloys with higher Mo dissolution and/or possibly attain binary Ni–Mo composites with higher bulk Mo without the same degree of sintering in the system. This would help extend our knowledge regarding the structure- function relationships in Ni–Mo systems. Also, preliminary unpublished calculations by Vishwanathan et al. to probe the electrocatalytic activity of Mo-incorporated fcc Ni surfaces for H_2 evolution revealed that near-optimal activity occurs between 25-50 mol% of surface Mo. This only reinforced our motivation for this study, given the potential for higher activity that can be derived via Ni–Mo composites obtained via a different synthesis.

It should, however, be noted that the inherent mechanism prevalent in the catalysts is unclear. A number of possible mechanistic hypothesis have been put forth for these systems. One possibility is that electronic interactions between Ni and Mo in the system result in improved H_2 binding energies, such that both the H_2 adsorption and desorption steps become facile.[74,87,88] Another possibility is the reduction in energy barrier associated with alkaline systems due to favorable interactions of the Mo–oxides present in the system with the water molecules thereby facilitating water dissociation. However, this hypothesis would not explain the concurrently high activity in acidic media. A third possibility is that

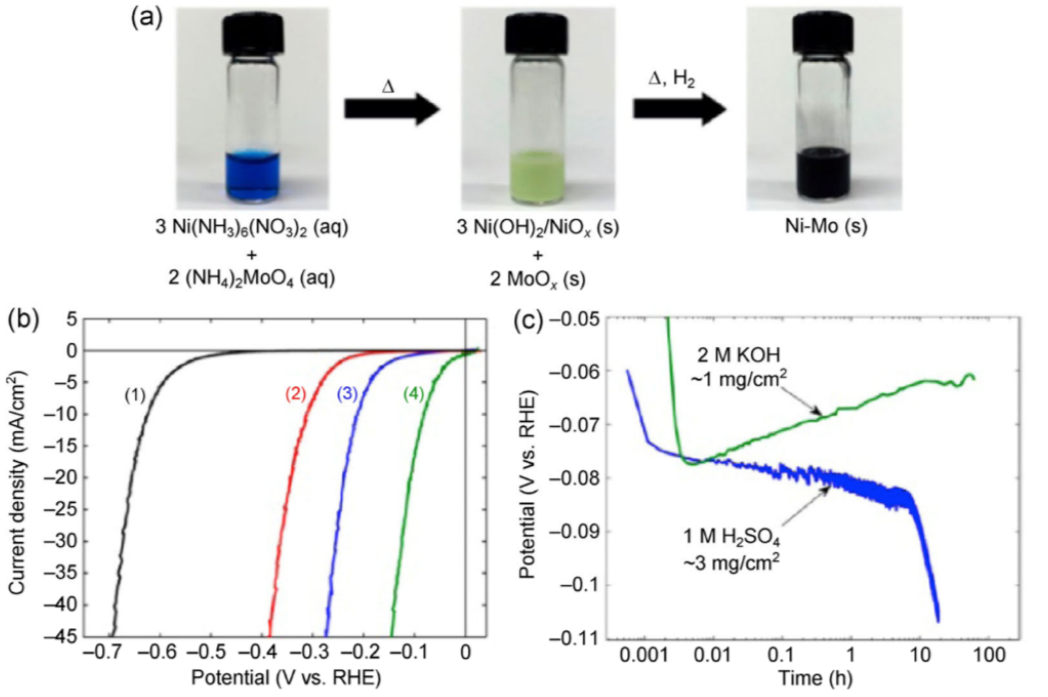

Figure 5: *(a) Illustration of synthetic processes with an initial precipitation step, followed by an annealing step under a reducing atmosphere. (b) Comparison of HER catalytic activities of (1) Ti foil substrate; (2) smooth Ni wire; (3) Ni nanopowder without Mo alloying on Ti foil (1 mg/cm^2); (4) Ni–Mo nanopowder on Ti foil (1 mg/cm^2) in 1 M NaOH solution with Ni mesh counter electrode and Hg/HgO (1 M NaOH) reference electrode. (c) Stability curves of Ni–Mo nanopowder on Ti foil (∼1 mg/cm^2) in 2 M KOH and (∼3 mg/cm^2) in 1 M H_2SO_4.Reprinted with permission from (McKone et al. ACS Catal. 3, 2, 166-169). Copyright (2013) American Chemical Society.*[70]

the increased activity of Ni–Mo over Ni is predominantly due to the increase in exposed surface area in the catalysts.[89] This is possibly true to some extent given the clear increase in porosity for these catalysts over that in Ni nanoparticles.

The final hypothesis that has been extended attributes the improved activity of Ni–Mo to unique surface chemistry characteristics - namely the formation of intrinsically more active hydride phases as argued by Conway while Highfield postulated a surface migration of these hydrides via a phenomena known as hydrogen spillover.[79,90] The lack of conclusive evidence to support or reject any of these hypothesis leaves open a significant scope for inferences. While we did not extensively investigate the mechanistic pathways associated with Ni–Mo systems. It was our hope that the use of a new synthetic pathway may shed some light beyond that achieved via the prior synthesis.

In summary, we wanted to identify a synthetic approach to produce high performing unsupported Ni–Mo nanopowders catalysts that would be amenable to scale up and possible commercial use in the future. An important parameter of this was to limit the toxicity of any by-products produced during the synthesis, like NH_3. Prior results had shown that structure–function–activity relationships could be leveraged to enhance the activity of these systems. The development of catalysts with alternate Ni/Mo ratios and different crystallographic order are important for elaborating on these relationships. It was believed that using an alternate synthetic route might be one of the avenues to change the composition and order of Ni and Mo in the final catalysts and hopefully provide further insight into the catalytic mechanisms prevalent in these systems.

2.2 "AMMONIA-FREE" NI-MO SYNTHESIS

The chemical method developed by McKone et al. for the synthesis of Ni–Mo nanopowders follows a two-step process involving initial precipitation of a mixed Ni–Mo oxide from a polyol solution, which can then be reduced under a H_2 atmosphere to yield black Ni-Mo powdered catalysts.[70] This solution phase synthesis of oxide powders is adapted from synthetic approaches developed by Levin et al.,who reported an aqueous precipitation of ammonium

nickel molybdate compounds from heating of ammoniacal mixtures of Ni(II) and molybdate salts in aqueous conditions,[91] and Schmitt et al., who proposed a polyol mediated synthesis for transition metal molybdate nanopowders accomplished simply by mixing the desired transition metal salt with $(NH_4)_2MoO_4$.[92]

The precipitation scheme is based on the fact that $(NH_4)_2MoO_4$ exhibit reasonable solubility in aqueous media, a characteristic atypical of other molybdates. Hence, the mixture of a soluble nickel salt and ammonium molybdate results in a double decomposition reaction generating insoluble mixed nickel molybdates that precipitate out of the solution.[93] The polyol media is expected to act as a stabilizer during the precipitation due to weak coordination to the surface of growing particles, resulting in small and relatively mono-disperse mixed oxides of Ni and Mo.[92] Such polyol-mediated precipitation approaches have gained popularity in recent times as a facile chemical synthesis approach for making metal nanoparticles.[94]

Another molybdate that exhibits such uniquely high solubility in aqueous media is Na_2MoO_4.[93] In fact, Pezerat and his coworkers, who first pioneered these solution based synthesis of first-row transition-metal molybdates, reported on the use of soluble metal salts and alkali metal molybdates to synthesize a series of phases having ideal formulas $MMoO_4 \cdot H_2O$,$AHM_2O(MoO_4)_2 \cdot H_2O$, and $A_{2-x}(H_3O)_xM_2O(MoO_4)_2$,where A = NH_4^+, Na^+, or K^+ and M = Zn^{2+}, Co^{2+}, or Ni^{2+}.[95,96] This work not only indicates that it is possible to use precursor molybdates that don't contain NH_4^+ cation but also that this synthetic approach can be used to prepare oxides with different M/Mo stoichiometric ratios.

Therefore, we sought to employ a precipitation scheme analogous to that by McKone et al., instead employing $NiCl_2$ as the nickel salt and Na_2MoO_4 as the metal molybdate in the precursor solutions. This would allow us to completely exclude NH_3 from the synthesis, instead generating a relatively benign NaCl byproduct along with the Ni–Mo oxides. The reaction scheme so proposed involved heating an equimolar mixture of $NiCl_2$ and Na_2MoO_4 in a water-diethylene glycol(DEG) polyol media, typically at metal concentrations $\sim$ 0.1-0.3 M to precipitate out a yellowish-green oxide phase, in a manner remarkably similar to the prior synthesis. These oxides were then purified through centrifugation with water and acetone and subsequently dried in an oven overnight to generate yellowish-green oxide

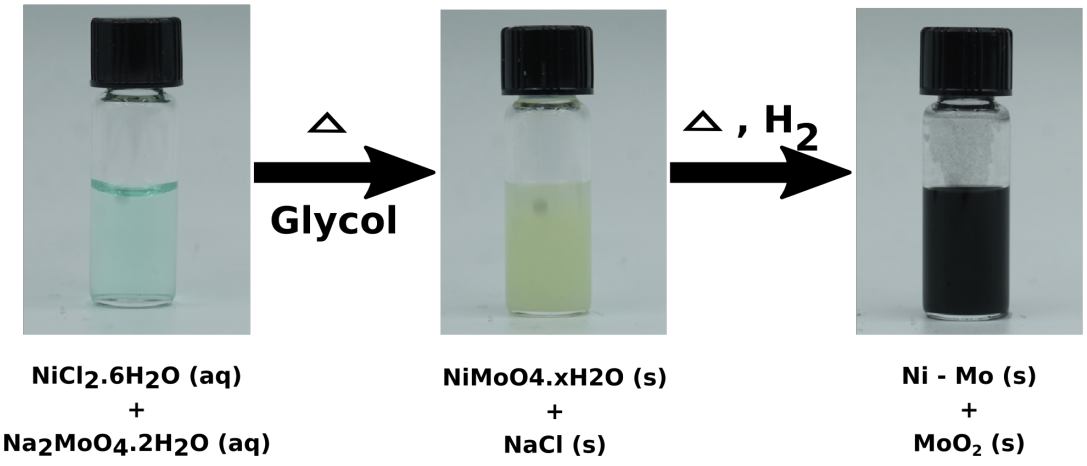

Figure 6: *Synthetic scheme for Ni–Mo nanopowders consisting of precipitation of* $NiMoO_4 \cdot xH_2O$ *from an aqueous solution of* $NiCl_2$ *and* Na_2MoO_4 *followed by thermal reduction under a* H_2 *atmosphere.*

powders. It was noted at this point that the oxide phase exhibited comparatively higher aqueous solubilities as compared to those produced in the prior synthesis. This was already a indication of the formation of an oxide phase different from the earlier synthesis, likely to be of alternate Ni/Mo ratios as compared to the prior synthesis. These powders were then annealed at 450°C under a H_2 atmosphere to reduce the oxides, yielding dry black catalyst powders. A typical synthetic scheme, illustrating the appearance and composition of the starting solution, intermediate oxide, and final catalyst material, is illustrated in Fig 6

Preliminary X-Ray diffraction (XRD) data was collected on oxide and catalyst powders using a Bruker D8 DISCOVER powder X-Ray Diffractometer with Cu K radiation(Kα1, λ= 1.5406Åand Kα2, λ= 1.5444 Å) to confirm the identity of the intermediate phase and final catalysts as illustrated in Fig 7. The diffraction spectra indicate the presence of pure phase nickel molybdate, $NiMoO_4$ as the intermediate oxide, implying the formation of an oxide with 1:1 Ni to Mo ratio prior to the reduction, as hypothesized. Interestingly, the identification of $NiMoO_4$ was complicated by the presence of lattice water in the intermediate phase. Hence,

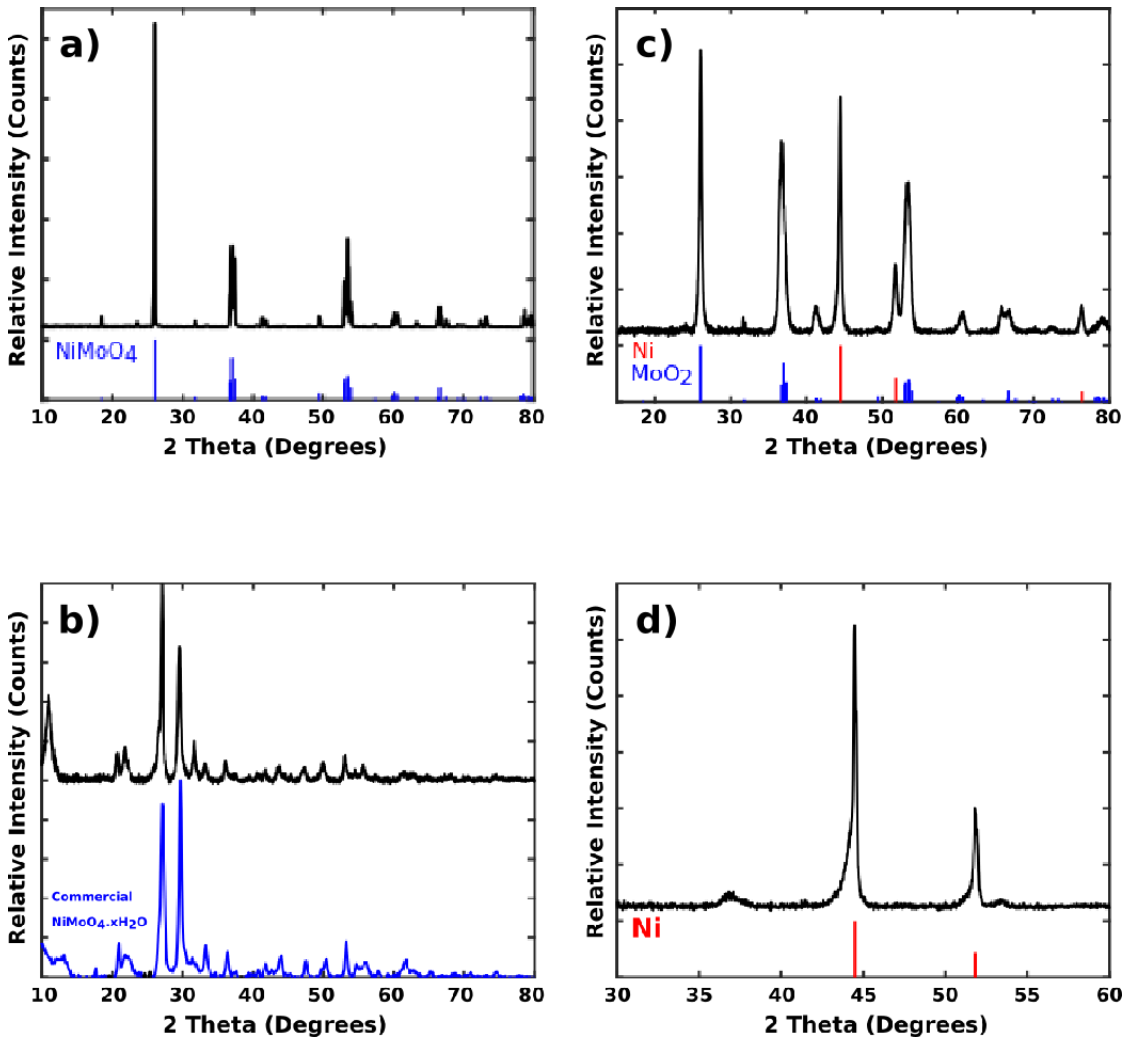

Figure 7: *Representative X–ray diffraction data for (a) the intermediate mixed oxide obtained from a typical nanopowder synthesis by dehydrating the oxides post purification (b) the intermediate oxides in their hydrate phase dried to powder form (c) final product from a typical synthesis (d) mixture of Ni and catalysts nanopowders illustrating the peak shift obtained on the Ni peaks*

the greenish-yellow powders of the intermediate oxide had to be dehydrated by heating in a muffle furnace set to 400°C for 30min prior to collection of the XRD data. In order to offer further confirmation, the XRD data for the hydrated phase was compared against that of a commercially obtained variant of $NiMoO_4$ Both XRD patterns gave a perfect match to the standard pattern for hydrated $NiMoO_4$, thereby confirming it as the intermediate product post precipitation in the synthesis. These $NiMoO_4$ are in fact quite common in both gas phase catalysis and electrochemistry literature.[97–100] They are known to be used as active catalysts for partial oxidation reactions, particularly for the selective oxidation of lower alkanes? and as electrochemical capacitors in novel energy storage applications.[99]

The XRD spectra for the final catalysts collected post reduction were then indexed to metallic MoO_2 and Ni with the Ni peaks broadened and slightly shifted to lower 2Θvalues indicating the formation of solid solution of Ni and Mo. This peak shift is more clearly illustrated in Fig 7(d) which shows the diffraction pattern for a mixture of Ni (as an internal standard) and catalyst nanopowders compared against the standard pattern for Ni. The peak shift represents a lattice parameter of 3.568Å, compared to 3.524Åfor pure Ni metal, calculated using the Scherer equation. Using the following experimental correlation reported by de Chialvo and Chialvo, the Mo dissolution in Ni lattice was estimated as $\sim 11 \pm 1\%$.[101]

$$a_o = 0.35242 + 0.00042 * (Mo), \tag{2.1}$$

where: a_o = lattice parameter of nickel (nm)

Mo = atomic percentage of molybdenum

This reflects a modest rise in the amount of Mo content in the synthesized alloy as compared to those reported by Csernica, who synthesized disordered $Ni_{0.92}Mo_{0.08}$ alloys from a pure aqueous precursor using the prior synthesis .[86]

The morphology of the intermediate oxide and final catalyst phases were imaged using scanning electron microscopy (SEM). As shown in Fig8, the $NiMoO_4$ in the intermediate phase exhibited one of three possible predominant morphologies. One predominant morphology was nanoparticulate aggregates with particle size varying between 50 and 100 nm. The second was a dense nanorod structure of similar size range and varying lengths. A third

observed morphology was a mixture of these two. A set of commercial $NiMoO_4$ powders were used as controls for the electrochemical and structural characterization studies, these however, consistently exhibited a nanorod structure.

Nanorod structures have been commonly reported in the literature for transition metal molybdates.[99,100] However we were able to find only one other example, by Saravankumar et al., who reported a similar structural diversity when synthesizing $NiMoO_4$ via co-precipitation of $NiCl_2$ and Na_2MoO_4.[102] They suggested that this structural variation is attributable to electrostatic interactions between Ni–Mo precursor anions with the cation head of the surfactant in the synthesis. The stabilizer used in our synthesis is uncharged but might exhibit similar structure directing properties due to its coordination to the surface of nucleating $NiMoO_4$ nanoparticles.

Alternately, Saravankumar also hypothesized that the aggregate structures might actually be a preliminary amorphous phase of $NiMoO_4$ that form before attaining definite crystal structure.[102] We tested this hypothesis via XRD analysis of two samples with these differing morphologies as presented in Fig9. In fact, the XRD pattern for the aggregated $NiMoO_4$ nanoparticles showed only very broad and low-intensity diffraction peaks, while the spectra for the nanorod structured oxides were narrower and well-defined. This result strongly supports the idea that essentially amorphous nanoparticles form first, followed by nanorods as the oxides begin to crystallize. However, this conclusion is somewhat convoluted by our limited understanding of the effect of lattice water on the XRD spectra of in these systems. Moreover, it does not clearly explain why some precipitates crystallized into nanorods, while others did not.

Our interest in precipitation dynamics and oxide morphologies was motivated by an initial assumption that the final catalyst material (Ni–Mo alloy plus MoO_2) would exhibit a morphology resembling that of the parent oxide. Remarkably, the final catalysts display far more consistent morphologies comprising aggregates of polydisperse particles tens of nanometers in size, along with somewhat larger platelet structures dispersed throughout the sample. As such the nanoparticle morphological growth during a typical synthesis could be described via the illustration in Fig 10. We were unable to distinguish compositional differences between these final particle and platelet morphologies due to their small size and

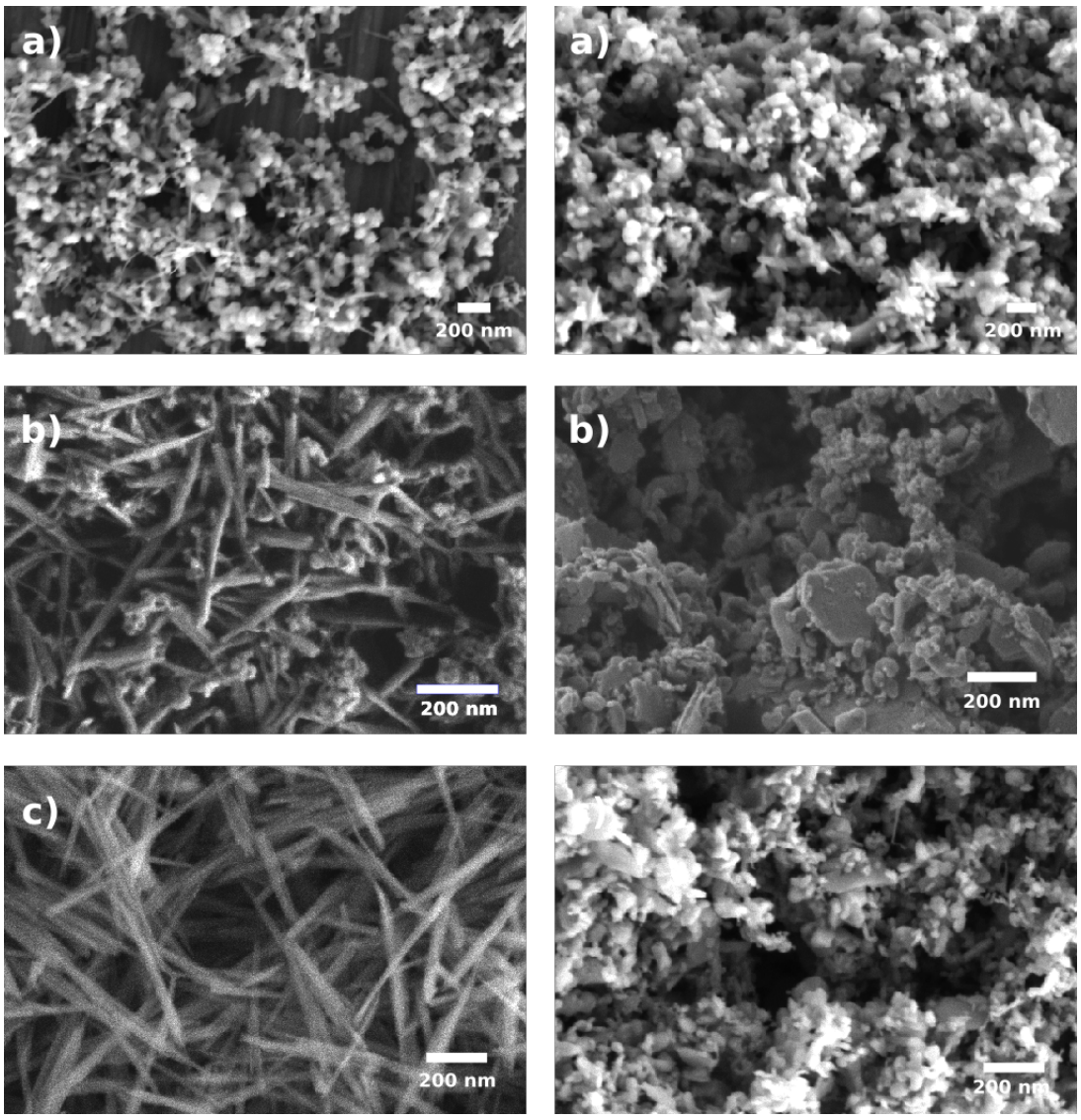

Figure 8: *Representative Scanning electron micrographs of (a) aggregated nanoparticulate structures of* $NiMoO_4 \cdot xH_2O$ *on the left and its reduced form on right (b) mixed nanoparticulate / nanorod structured* $NiMoO_4 \cdot xH_2O$ *on the left and its reduced form on right (c) nanorod structured* $NiMoO_4 \cdot xH_2O$ *on the left and its reduced form on right*

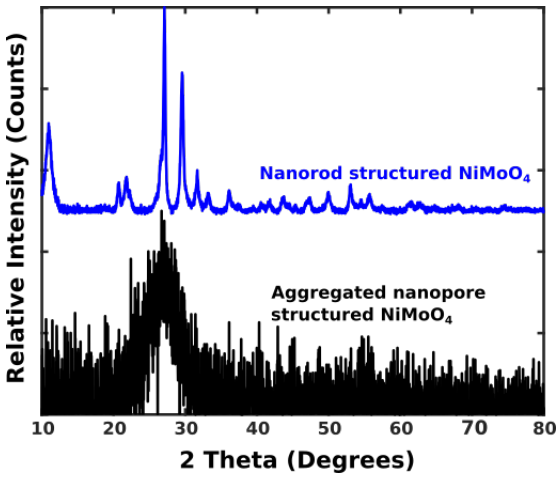

Figure 9: *Representative X-ray diffraction data for (top) nanorod structured* $NiMoO_4 \cdot xH_2O$ *(bottom) nanopore aggregate structured* $NiMoO_4 \cdot xH_2O$

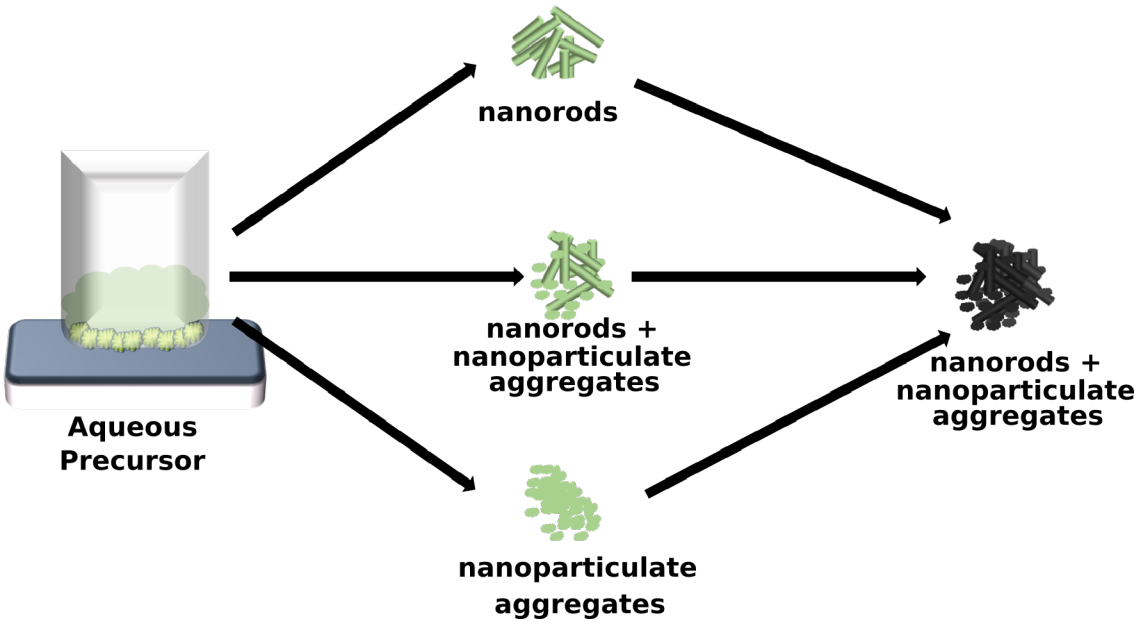

Figure 10: *Representative morphological growth of nanoparticles over precipitation and reduction steps (left to right)*

high degree of aggregation; thus, the possibility remains that the mixed final morphology reflects two compositionally discrete components, where one or both may be necessary for catalytic function.

As noted previously, glycol is thought to mediate small particle growth through surface chelation, but a mixture of glycol with water was used since the solubilities of the precursor materials in glycol are too low to use a pure glycol system. However, it was also observed that the $NiMoO_4$ formed as the intermediate stage has significant solubility in water. Since an overarching goal of our work was to improve the processability of these catalyst systems, it was imperative to quantify the solubility of $NiMoO_4$ as well as calculate and possibly optimize the oxide yields from the synthesis.

In order to calculate the aqueous solubility of $NiMoO_4$, we first prepared a series of solutions of $NiMoO_4$ in deionized water with concentrations ranging from 0-8 mg/ml as shown in Fig11, left. These solutions were stirred overnight to allow sufficient time for all the possible solute to dissolve. It was noted that at concentrations above 3mg/ml, a portion of the $NiMoO_4$ added to the system remained un-dissolved. This was assumed to be the tentative saturation limit for $NiMoO_4$ in water. Based on the increasing coloration of the solution at increasing concentrations of $NiMoO_4$, we decided to employ UV–Vis spectroscopy to estimate the exact solubility of these oxide powders. Through support from Dr.Veser's research group we collected the UV–Vis spectra for the entire range of solutions prepared, plotting relative absorbance as a function of wavelengths between a 350-900nm range. The relative absorbance values are expected to be a function of the concentration of $NiMoO_4$ in the solution. In a deviation from the prior result, the UV–Vis data demonstrated a monotonically increasing concentration of solute($NiMoO_4$) in water, well beyond the previously estimated 3mg/ml as illustrated in Fig11, right. Hence, the saturation concentration of $NiMoO_4$ could not be assumed to be 3mg/ml since the UV-Vis data clearly showed that there is at least a higher degree of solvation of $NiMoO_4$ in water when more solute is added, even though all of it does not seem to dissolve.

One explanation for these puzzling observations is that the timescale for dissolution of $NiMoO_4$ in water are very long, in which case it would not severely affect our synthesis. However, this does not seem to be the case since we have found separately that oxide yield

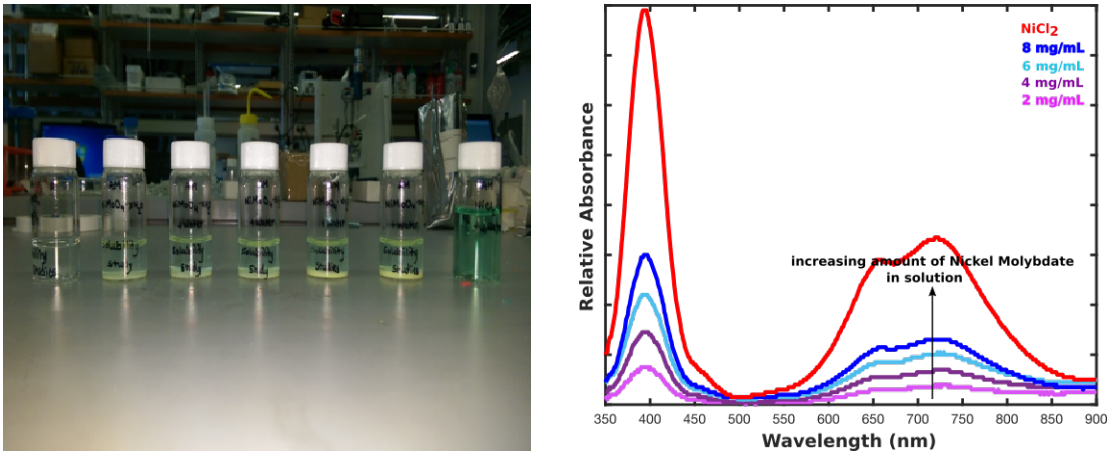

Figure 11: *(left) Samples prepared with increasing amounts of dissolved $NiMoO_4$ from left to right. (right) analogous UV-VIS data plotting relative absorbance for each sample between a 350nm to 900nm. The relative absorbance is expected to be a function of the concentration of $NiMoO_4$ in solution.*

decreases substantially for each purification step that we employed using a water wash. The solubility might instead obey more complex solvation dynamics that cannot be extracted from simple UV–Vis data.

Nevertheless, the oxide yield from a typical precipitation step was evaluated to be 35% on a mass basis.

$$Yield = \frac{Mass\ of\ \mathrm{NiMoO_4 \cdot xH_2O}\ retrieved}{Mass\ of\ \mathrm{NiCl_2 \cdot 6\,H_2O} \quad + \quad Mass\ of\ \mathrm{Na_2MoO_4 \cdot 2\,H_2O}} \tag{2.2}$$

The final catalyst yields for a typical synthesis amounted to 35% on a mass basis. During the course of our work with these systems, it was further observed that the glycol content had a strong effect on the oxide yield. Hence, we measured catalyst yield over a range of increasing amounts of glycol in the synthesis—these data are shown in Fig12. They show that oxide yields rise to $\sim$ 40% at glycol contents of 50% within the solution.

Although a maximum yield was not found within this range, it was deemed counter-productive to raise the proportion of glycol in the synthesis to a large extent. The precipitation step is based on the differential solubilities of the precursor and precipitated phases

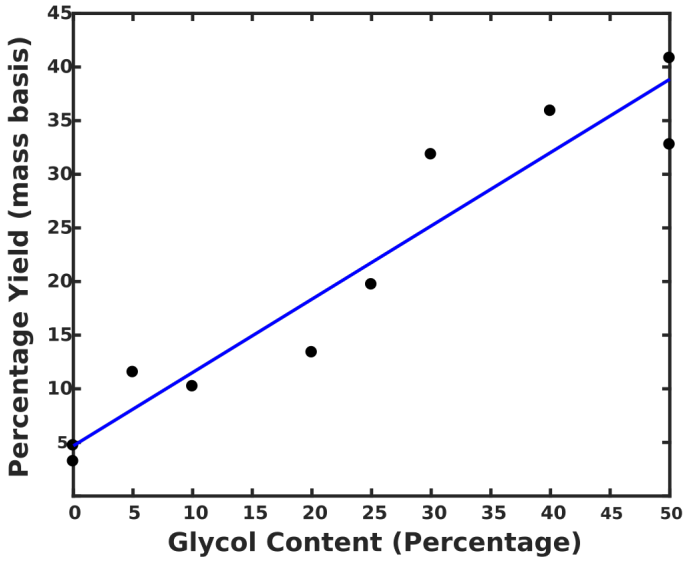

Figure 12: *Representative data for calculated percentage yield derived form increasing concentrations of glycol in the precursor.*

and the solubility of the precursor salts is minimal in glycol hence the synthesis will then become limited by the solubilities of the precursor salts in glycol/water mixtures.

The second step in the catalysts synthesis process is the thermal annealing of the precipitated oxides at temperatures around 400-500°C under a forming gas(5% H_2 , 95% N_2) flow. This results in the removal of a significant quantity of O_2 as water vapor, thereby resulting in a large volume reduction in the solid, creating void spaces. These voids are believed to enhance the activity of the catalysts through the availability of a higher surface area in the active catalyst. The as-synthesized powder was mildly pyrophoric upon removal after the reduction step, suggesting that it might is prone to oxidation in air. The powders were instead allowed to undergo slow surface oxidation prior to removal to allow for safe retrieval of the dry powders after the reduction.

Ni nanopowders were synthesized using the same procedure in the absence of molybdenum salts in the precursor. Pt nanoparticles on carbon supports were synthesized in–house by an aqueous ascorbate reduction method under development by other McKone lab researchers. (see Ch4)

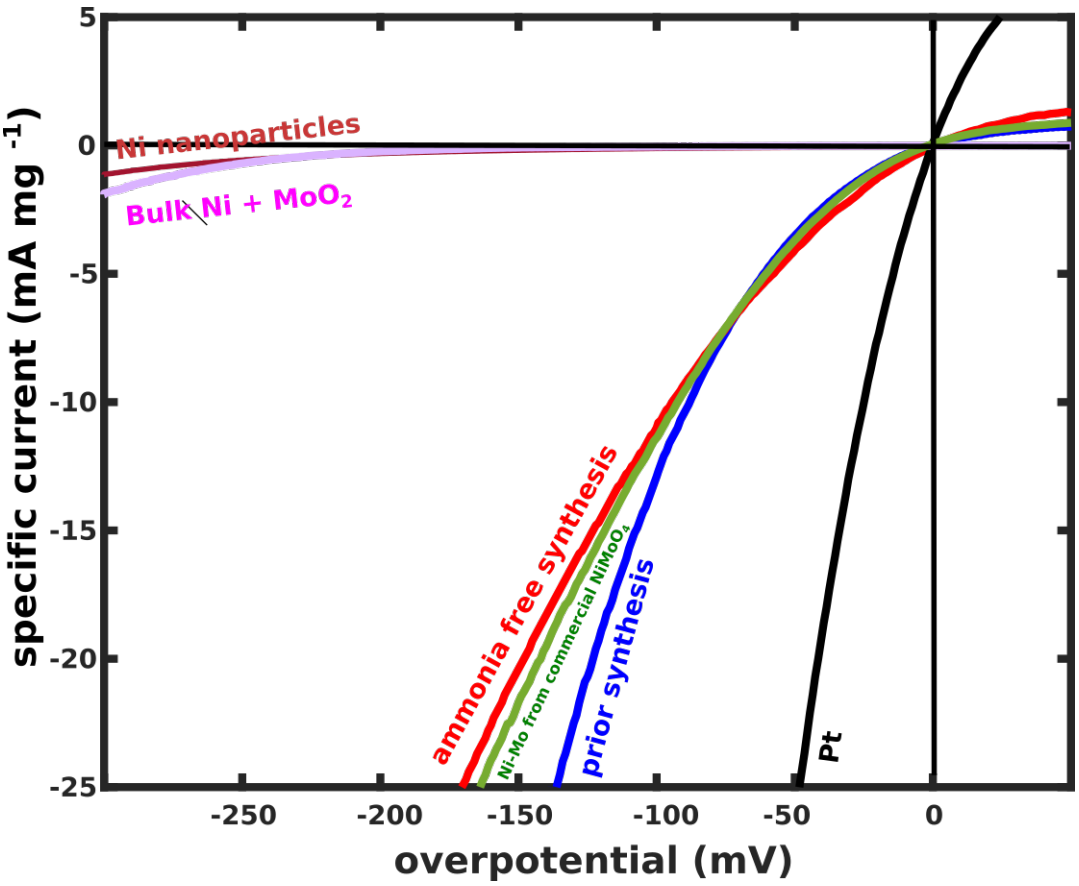

Figure 13: *The comparison of HER catalytic activities reported as an average of the forward and reverse peaks of the reported catalysts in H_2 saturated 0.1M KOH aqueous solution estimated using electrodes with mass loadings of ∼0.4 mg/cm^2 on Ti substrates. Data was collected using a three–electrode cell setup and an Ag/AgCl reference. Contact and solution resistances were compensated using the positive feedback method, with IR resistances ∼20-30 ohms. "Bulk Ni+MoO2" refers to nanopowders of Ni and MoO_2 mixed together as a paste. prior synthesis refers to the Ni–Mo nanopowders synthesized via ammoniacal solutions of Ni and Mo salts as reported by McKone et al. "Pt" refers to the platinum on carbon nanoparticles synthesized by Dean Miller.*

The hydrogen evolution activity of these Ni–Mo nanopowders were evaluated under alkaline conditions using 0.1M KOH as shown in Fig13. For Ni–Mo loadings of 0.1mg on 0.25 cm^2, the as synthesized Ni–Mo catalyst systems exhibited mass specific HER activities of $\sim$10 mA/cm^2 at 100 mV overpotential. This was markedly higher than the HER activity of pure Ni nanoparticles and essentially similar to the activity derived from Ni-Mo nanopowders synthesized via the ammonia-based method reported previously.[70] The catalysts produced by reducing commercially obtained oxides also exhibited similar activity to systems synthesized by our water/glycol precipitation method, which further supports that the composition and morphology of the final catalyst was rather insensitive to those of starting material.

An expression that can be used to describe the heterogeneous electrode kinetics in these systems is the Tafel equation shown below.

$$i = i_0 * 10^{\eta/b}$$

At higher potentials wherein either the reduction or oxidation reactions are dominant over the reverse reactions, it equates the observed reaction rate, i (expressed in terms of current density in electrochemistry as per Faraday's law) to the product of the exchange current densities, i_0 (the intrinsic electrocatalytic rate constant of the reaction — a measure of the equivalent rates of the forward and reverse reactions under dynamic equilibrium) and the exponential function of the overpotential,η, normalized to another characteristic constant, b called the Tafel slope. The Tafel slope being a measure of the sensitivity of electrocatalyst turnover to an increase or decrease in applied overpotential.

An agreement of the hydrogen evolution behavior of the catalyst to this equation reflects a kinetically controlled reaction. The presence of an exponential drop in current densities at potentials over the onset potentials in HER systems can be used as a cursory assessment for agreement of electrochemical behavior to the Tafel law. This is observed in Pt systems as demonstrated in Fig13. The hydrogen evolution data of the Ni–Mo catalysts, however, demonstrated a deviation from the typical Tafel behavior, the curve becoming increasingly linear behavior at higher overpotentials (see Fig13).

This would indicate that the hydrogen evolution activity of Ni–Mo in alkaline media is not only kinetically limited but also has other activation barriers like transport or electron

transfer resistivity. It was posited that the Mo-oxide phases in the catalysts could result in the presence of resistive interfaces within the catalyst. This electrical resistance will then dominate the observed current flow at some overpotentials especially at high current densities. This effect is all the more pronounced for active catalysts such as Ni–Mo since they achieve high current densities at low overpotentials. As per the HER data shown in Fig13 this resistive effect is more pronounced in the Ni–Mo catalysts derived from ammonia–based syntheses as compared to those from the prior synthesis. (more discussion available in Chapter5)

Interestingly, if the linear behavior at higher current densities is in fact due to a high interfacial resistance between individual catalyst particles, it would imply that these systems ,in fact, have even higher intrinsic catalytic activity than what we have observed. Nevertheless, bulk conductivity may impose a practical limitation in functional catalyst materials, just as mass transfer limitations do in gas-phase systems. These limitations have been previously noted as important in semiconducting catalyst materials like MoS_2, but they have not been clearly observed in nominally metallic materials.[6]

It was noted that during multiple synthetic runs of these catalysts that it was difficult to consistently obtain the same mass-specific HER activity. It was posited that the observed variation in the activities might be rooted in the morphological variations observed for the intermediate oxides during synthesis. Indeed, sulfidized Ni–Mo composites are known catalysts for hydrodesulferization (HDS), and there are a number of reports in the HDS literature regarding the limited reproducibility of $NiMoO_4$ precursor synthesis. For example, Mazzocchia C. et al. reported that small changes in synthetic conditions like pH, molarity and precipitation time, duration of aging of the precipitate have a notable effect on precipitation product.[?] These experimental conditions are challenging to control, especially across multiple synthetic runs in the simple benchtop batch synthesis that we have employed. The activity reported in Fig13 was derived from systems made by exactly mimicking the synthesis reported by McKone et al. in order to draw consistency. A much more expansive discussion on the effect of precipitation dynamics on catalyst activities is presented in Ch3.

The operative mechanism of Ni–Mo alloy HER electrocatalysis is still essentially unknown. As such, it is also unknown whether the higher activities over pure Ni arises out of interactions between alloyed Ni and Mo or whether closely interacting bulk mixtures of Ni and Mo might be sufficient to elicit the activity enhancement we observed in these systems. Another possible hypothesis is that the MoO_2 present in these systems might be critical to the activity enhancement. Thus, modest attempts were made to further elucidate the synergistic mechanisms prevalent in these catalysts.

In order to gain a better understanding of the composition and morphology of these catalysts, we first executed scanning transmission electron microscopy (STEM) and energy dispersive spectroscopic (EDS) analysis of the as–synthesized Ni–Mo catalysts with the help of Stephen House of Judith Yang's group. High definition imaging was completed using a JEOL JEM-2100F Transmission Electron Microscope (TEM) with Gatan GIF-Tridiem, EELS and Oxford Inca XEDS. The micrographs from the HAADF STEM imaging and the elemental maps from the STEM EDS are presented in Fig14.The quantitative information associated with these elemental maps are summarized in Table1 as ratios of Ni, Mo and O relative to one another over the entire sample as well as two prevalent regimes within the sample, named as the Ni–rich and Ni–poor regions. These have been differentiated based on the relative ratios of Ni:Mo prevalent in these regions. The Ni–rich regions exhibit the presence of a 4:1 ratio of Ni:Mo while the Ni–poor region is made up of a $\sim$1:4 ratio of Ni:Mo. It was posited that these systems could be described as localized collections of alloyed Ni–Mo nanoparticles with a Mo–oxide rich envelope around it, most likely MoO_2. This is based off the final catalyst composition revealed in the XRD (see Fig7) analysis. While this might be tentatively true, there is definitely some dispersed Ni also present in the Mo–rich region, whether as Ni, Ni–Mo nanoparticles, NiO, unreacted $NiMoO_4$ or maybe even some mixture of these, it is difficult to ascertain.

Similar TEM studies were conducted previously by Rituja and Stephen on Ni-Mo systems synthesized by the prior synthesis, the results of which are presented in Fig15. Interestingly, these systems also exhibited similar aggregated morphologies, however, their systems demonstrated the presence of multiple fairly discrete core-shell structures of Ni-rich cores enveloped by a Mo-oxide shells (more clearly illustrated in Fig15, right). This was indicative

Table 1: *Typical elemental ratios of Ni, Mo and O within the Ni-rich , Ni-poor regions and over the entire sample as estimated using energy dispersive spectroscopy. The standard deviations account for the variability in these ratios due to variation in density at different points within the sample*

	Ni/Mo	**O/Ni**	**O/Mo**
Overall	0.7 ± <0.1	9.9 ± 0.9	6.7 ± 0.6
Ni-rich region	3.9 ± 0.1	1.2 ± 0.1	4.6 ± 0.4
Ni-poor region	0.3 ± <0.1	23.6 ± 2.3	6.2 ± 0.6

that the Ni–Mo and MoO_2 were both fairly dispersed all across the sample while maintaining this core-shell architecture unlike the predominantly localized presence of the Ni–Mo in our systems.

More importantly, this would imply that the surface of contact between the Ni–Mo and MoO_2 in both systems is expected to be widely different. This feature has been demonstrated in Fig.16. Given that Ni–Mo catalysts demonstrate similar hydrogen evolution activity (see Fig13) irrespective of the synthesis route, the above result would support the conclusion that the Ni–Mo alloy is the active site during the catalysis and the MoO_2 does not actively participate in catalyzing the reaction. It is however, possible that the Mo oxide matrix serves as a as a reservoir for Mo during formation of the Ni-Mo alloy phase, and it may also minimize sintering Ni-rich particles during thermal reduction. On the other hand, it may also inhibit physical transport of reactant species to the active Ni-Mo catalyst, thereby influential in producing these active catalysts finally. Hence, it is imperative to extend our understanding of the significance of this MoO_2 component of the catalysts.

In order to do so, we synthesized pure MoO_2 and Mo via prolonged reduction of MoO_3 under H_2 gas at high temperatures. The resulting MoO_2 or Mo were co-dispersed with independently synthesized Ni particles in isopropanol. However, the prolonged reduction synthesis might have resulted in extremely large particle size for MoO_2 and Mo. This conclusion was supported by simple experimental observations such as the poor dispersion of these particles in isopropanol and their limited adhesion to the Ti substrate without the help

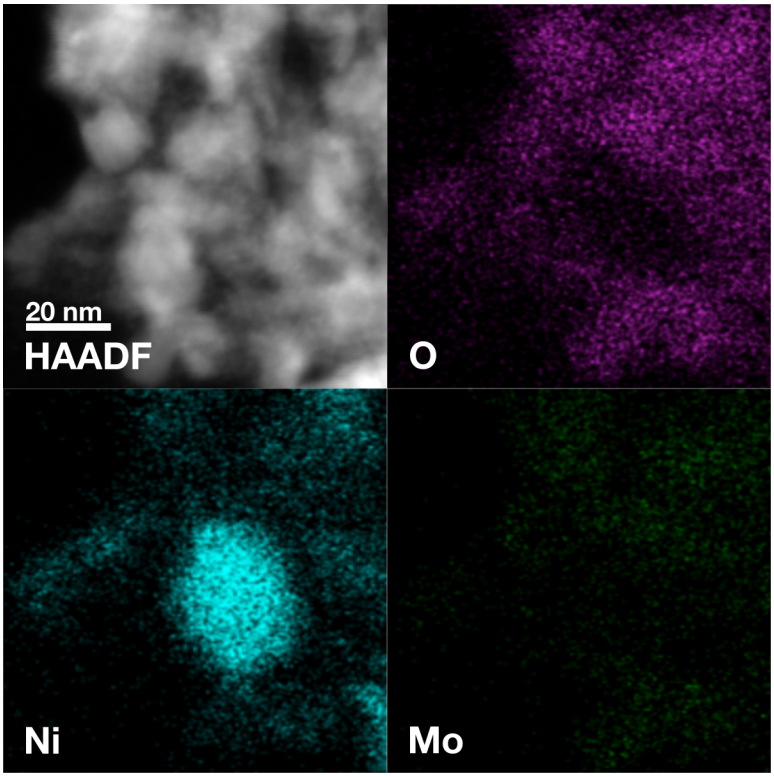

Figure 14: *Scanning transmission electron micrograph (top, left) and Energy dispersive spectroscopy maps for Ni–Mo nanopowders synthesized using the "ammonia-free" synthesis*

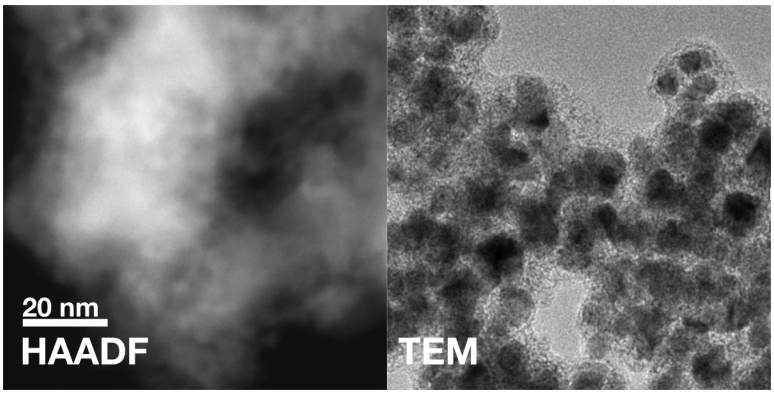

Figure 15: *Scanning transmission electron micrograph(left) and transmission electron micrograph(right) of Ni-Mo nanopowders synthesized using the prior synthesis)*

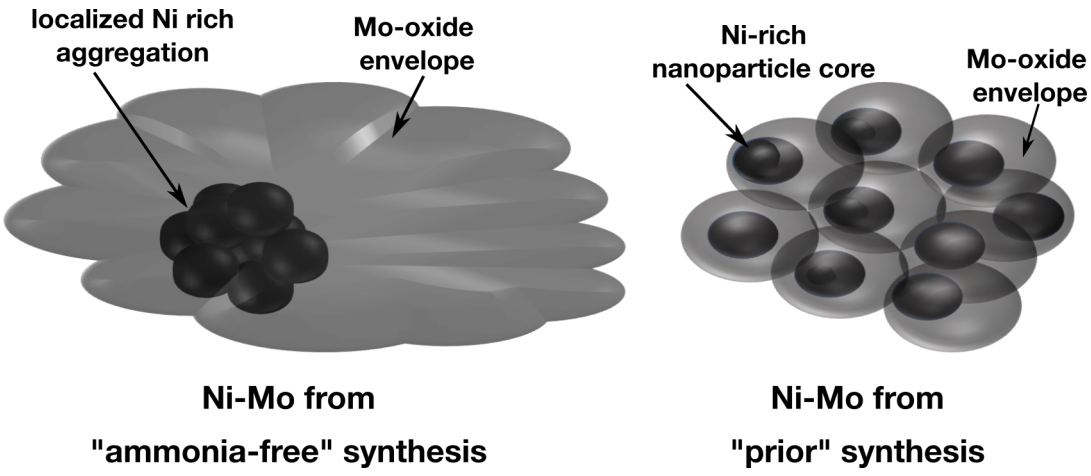

Figure 16: *Illustration of different morphologies of Ni–Mo systems as synthesized from the two synthesis methods*

of adhesive polymer additives like nafion. The HER activity of these systems were tested in the same setup as before. It was found to be similar to that shown by the Ni component alone. This could have been indicative of a lack of bulk activity enhancement between Ni and MoO_2 or Mo. However, we also noted that some of the catalyst leaches into the electrolyte, in which case the activity being exhibited could simply be that of Ni alone. Other attempts to synthesize nanopowder catalysts via co-reduction of NiOH and MoO_3 or MoO_2 on Ni foils were also largely unsuccessful due to the lack of control over particle size via these simple synthetic approaches.

2.3 CONCLUSIONS

In conclusion, we have been able to present an alternative synthetic approach for producing Ni–Mo nanopowders without the use of NH_3 as a solubilizing additive or compromising on the over all HER activity of these systems Thus, this synthesis is more amenable to commercial scalability and potential incorporation into a continuous synthetic approach, which is of considerable interest for future work. The success of this approach also provides a broader

validation of the generality of the synthetic approach developed by McKone et al. towards synthesizing active Ni–Mo nanopowder catalysts. Additionally, we have been able to identify a synthetic pathway wherein the intermediate oxides have a 1:1 ratio of Ni to Mo with a well-ordered structure. This could be leveraged in later studies to pursue Ni–Mo catalyst systems with higher levels of Mo enrichment, and therefore higher activity. We found that the synthetic parameters for the precipitation synthesis of $NiMoO_4$ have an appreciable effect on intermediate morphologies and possibly also final catalyst activities. Further, the TEM imaging done on these catalysts elaborate the morphology and compositions of the final catalysts while lending support to the hypothesis that the Ni-Mo alloys might be the active sites for the catalysis in these systems. Lastly, the HER activity of Ni-Mo nanopowders displays deviations from Tafel behavior at higher current densities, indicative of electrical conductivity limitations in the system.

Moving forward, it will be important to pursue stability studies on this new catalyst synthesis to lend further support to the applicability of this approach in place of the ammonia–based synthesis. It will also be important to identify the critical parameters in the catalyst synthesis that have the most significant effect on final HER activity. These results could then be used to optimize the synthetic strategy for these material to give smaller or more porous catalysts, resulting in higher active surface area and consequently HER activity. Some initial efforts to this effect will be discussed in the next chapter. Also, elucidation of the synergistic mechanism between Ni and Mo is worthwhile in the interest of improving intrinsic catalyst activity further. Three first step towards this could be the via leaching of MoO_2 in aqueous base. This will help assess whether the Mo in the alloy phase or the MoO_2 is more important for the enhanced activity. This leaching process is also anticipated to reduce the transport limitations due to the presence of the MoO_2 matrix that surrounds much of the Ni–Mo alloy particles in the final catalyst.

3.0 EVALUATING STRUCTURE–FUNCTION–ACTIVITY RELATIONSHIPS IN NI–MO NANOPOWDER CATALYSTS

3.1 INTRODUCTION

This chapter describes our study of the effect of structural and compositional variations on electrochemical activity of Ni–Mo electrocatalysts developed as per the synthesis described in Ch2. The purpose of this study was to leverage this knowledge in enhancing the final activity of these catalysts as we attempt to develop the most active Ni–Mo systems.

We first attempted to identify the relationships between the various process parameters of the synthesis and the final HER activity. This was motivated by our characterization studies on these systems(see Ch2), which showed that minor variations in the synthesis effected variations in the morphology of the intermediate phase and activity of the final catalysts. A better understanding of these changes could be used to improve the structure and composition of these systems (i.e., by delivering the optimum Ni/Mo ratio and maximal surface area) and thereby improve overall mass specific activities of these systems. Moreover, a complete understanding of the salient synthetic parameters is important to meet our long–term goal of scaling the production of these catalysts. Synthetic parameters from our batch reaction approach could be used to help inform process design for a large-scale continuous synthesis process. Therefore, we focused on characterization of the precipitation and reduction dynamics.

We also explored the potential for activity enhancement through the addition of dopants and additive supports into these Ni–Mo systems. This was attempted through catalyst doping of Ni–Mo with Ru based on a chemical analogy between the redox chemistry of Ru and Mo. We finally tried to address activity limitations arising from low bulk conductivity

in final Ni–Mo catalysts using graphitic carbon black additives. I collaborated closely with Rituja Patil during the course of this work. Rituja primarily focused on enhancing the activity of Ni–Mo systems derived via the prior synthesis and hence pursued many similar lines of experimentation. She was particularly integral in elaborating the effect of carbon additives in limiting the bulk conductivity concerns in Ni–Mo electrocatalysts.

As previously discussed, Ni–Mo alloys are already among the best earth–abundant catalysts for the HER under alkaline conditions, however its overall mass specific activities still lag behind that of industrial benchmarks achieved by Pt in acid. There are, however, some common strategies that are often adopted to improve the HER performances of catalysts in alkaline mediums. These strategies have been well encapsulated in a review paper by Mahmood et al.[?] and described in the following sections. These strategies formed the guiding principle for much of the work described in this chapter. We employed straightforward measures that intersect on each of these strategies in order to improve the HER performance Ni–Mo catalysts. We predicted that these approaches would help us further close the performance gap between precious and non-precious HER catalysts.

3.1.1 Optimization of macro morphological properties of catalyst

Morphological characteristics like total active surface areas and porosities play an important role in defining electrocatalytic activity. Nanostructuring is an effective approach to improve observed current density at the same overpotential by increasing the accessibility of reactants to active surfaces.[61,68] We hypothesized that limiting the particle sizes of Ni–Mo catalyst through better control of the nucleation and growth processes during oxide precipitation could result in higher surface area and consequently improved HER activity yields for these systems. Also, Csernica et al. showed that introducing structural order in Ni–Mo HER catalysts might result in higher intrinsic activities upon normalization with surface areas.,[86] but these results were convoluted by variations in available surface area. Thus we sought to better control synthetic conditions so as to achieve similar particle sizes while systematically varying other parameters in the batch precipitation reaction.

3.1.2 Optimization of chemical composition

The chemical composition of the catalysts is the defining factor in influencing their intrinsic activities. Thus, the identities and ratios of metallic elements in binary or ternary alloys are important factors during electrocatalyst design.[66,103] It has already been observed that variation in the alloy or bulk Mo content in Ni–Mo systems has an effect on its HER activity. Again, we hypothesized that a change in the Ni/Mo ratios of the oxide intermediate would allow us to access alloy systems with higher Mo dissolved into the alloy lattice and therefore show improved HER activities.

3.1.3 Developing hybrids with carbonaceous materials

Good electrical conductivity and a homogeneous dispersion of catalysts are also important to HER catalyst performance.[104,105] Poor electrical conductivity due to interfacial resistivity between catalyst particles results in voltage drop across the electrode, resulting in additional overpotentials and leading to lower apparent catalytic activity.[106] This phenomenon was already observed in these Ni–Mo systems, specifically illustrated by the deviation in exchange current densities from Tafel behavior at higher overpotentials as well as the marked increase in activity through an "activation" step comprising thermal reduction after catalyst deposition on Ti substrates, which was thought to improve adhesion and electronic conductivity of the catalyst layer.[9] Carbon materials, such as Vulcan carbon black, carbon nanotubes (CNTs), or graphene are known to increase the conductivity of hybrid catalysts and also increase their dispersion, which allows full use of exposed active sites.[49,107–109] This approach has been used in the past to improve the activity of Mo sulfide HER catalysts that showed low conductivity within the catalysts since they are semiconductors instead of metallic conductors.[6,110,111]

3.2 EFFECT OF PRECIPITATION DYNAMICS

The co-precipitation technique for synthesis of metal molybdates is a relatively facile approach that is used quite commonly.[97] However, this method has been noted to lack reproducibility, the precipitate being strongly dependent on the precipitating conditions.[112] A similar lack of reproducibility was observed during the course of our characterization studies (see Ch2) wherein a range of different oxide morphologies were observed under limited control of the process parameters. This was believed to be linked to incidental variations in the specific conditions of the precipitation reaction. Hence, we sought to systematically study the effect of a range of reaction parameters on the intermediate oxide and catalyst morphologies as well as the final observed HER activity.

The co-precipitation reaction is expected to proceed via a nucleation and then a growth step during the formation of $NiMoO_4 \cdot xH_2O$. The nucleation step is expected to be dependent on the concentration of the precursors in the synthesis while the precipitation time was expected to control the length of the growth or aging step in the precipitation once the nucleation occurs. Thus, we hypothesized that optimization of these parameters would afford us a higher degree of control over the final morphologies of the intermediates produced.

First, we sought to accomplish a controlled variation of the precursor concentrations while keeping all other synthetic parameters constant. Hence, we prepared four samples wherein the total metal concentrations in the precursor were varied from 0.05M to 0.3M by using increasing amounts of $NiCl_2$ and Na_2MoO_4 in the precursor solution during the synthesis. The molar ratio of $NiCl_2$ and Na_2MoO_4 was however kept consistent at 1:1, as were all other parameters of precipitation - precipitation time at 2min, hotplate temperature at 500°C. A strong effort was maintained to employ the same techniques during the addition of precursors, precipitate retrieval and drying and then subsequent reduction.

Preliminary evaluation of these samples was done on the basis of change in the HER activity of the final catalyst brought about by the changing precursor concentrations. The catalysts exhibited a monotonic increase in catalytic activity as shown in Fig17. We noted, however, that the increase in activity was modest, exhibiting less than two–fold higher HER activity at 150mV overpotential over a six–fold increase in precursor concentration.

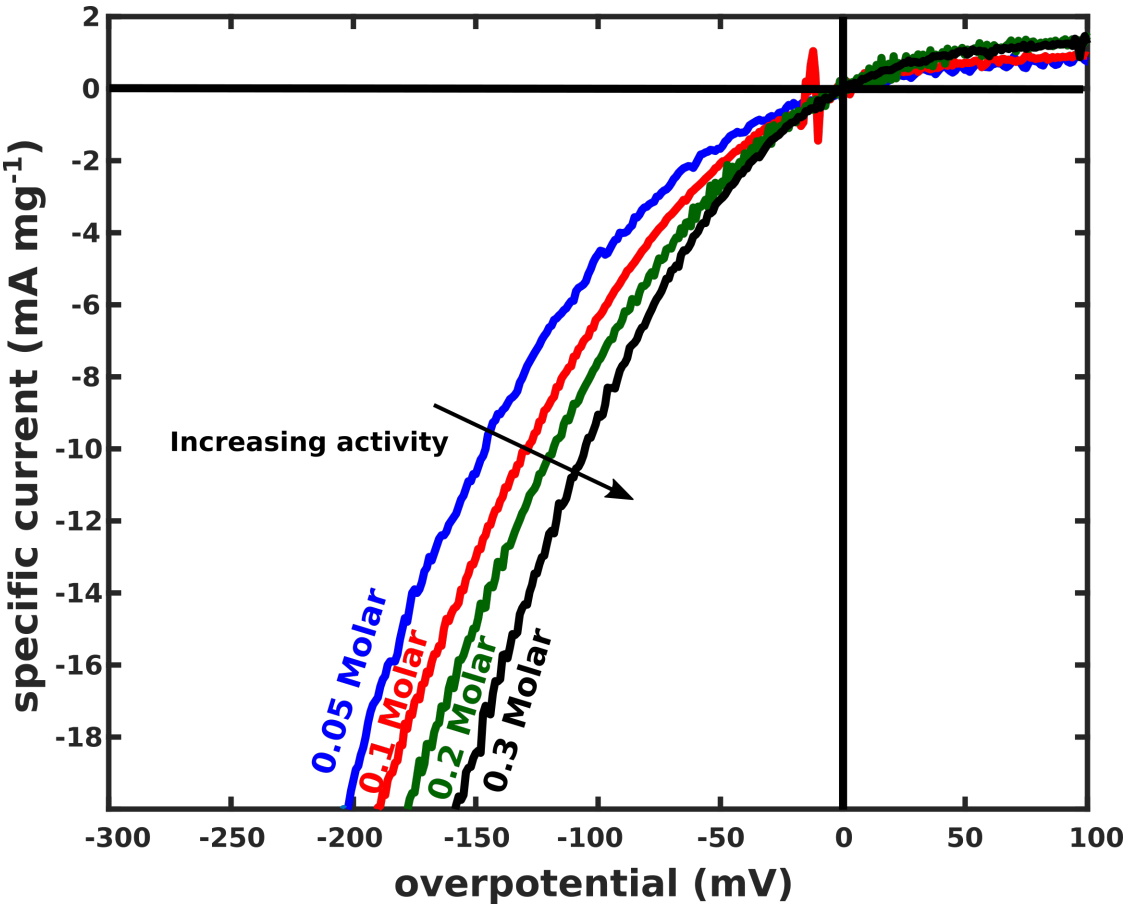

Figure 17: *The comparison of HER catalytic activities of catalysts made from different molar concentrations of precursor solutions reported as an average of the forward and reverse peaks of the reported catalysts in H_2 saturated 0.1M KOH aqueous solution estimated using electrodes with mass loadings of ∼0.4 mg/cm^2 on Ti substrates. Data was collected using a three electrode cell setup and an Ag/AgCl reference. The contact and solution resistances were compensated using the positive feedback method, with IR resistances ∼20-30 ohms.*

To better understand the origin of improved HER activity with increased precursor concentration, we carried out SEM analysis, the results of which are shown in Fig18. These data reveal the formation of what was previously noted as amorphous oxide particulates at concentrations below 0.2M and crystalline nanorod structures at higher concentrations. There were, however, very few observable differences in the morphologies of the final catalysts, which all exhibited aggregated particulate morphologies irrespective of the morphologies of $NiMoO_4$ intermediate phases.

During the synthesis of $NiMoO_4$, Kianpour et al. had reported a similar dependence of $NiMoO_4$ morphologies on concentrations while using $(NH_4)_6Mo_7O_{24} \cdot 4\,H_2O$ and $Ni(C_7H_5O_2)_2$ as precursors and PEG as a surfactant in the synthesis. They noted that the non-ionic surfactant was influential in determining the precipitate morphologies.[100] More recently, Saravankumar et al. reported a variation in the morphologies of $NiMoO_4$ precipitates observed the formation of nanorod / nanoparticulate morphologies under varying concentrations while using the same precursors as us but an ionic cetyl trimethyl ammonium bromide (CTAB) stabilizer. He rationalized the difference in morphologies as being dependent on the ratio of the precipitate and the stabilizers as the interactions between the precipitate and the stabilizers in the synthesis control precipitate morphologies.[102]

The DEG stabilizer used in our synthesis is known to influence particle growth through weak coordination on growing precipitate, hence, it might be that the change in the glycol/precursor ratios might be resulting in this difference in growth dynamics. There is however, an excess of glycol in the synthesis of all four samples studied here and thus it would be surprising if such minor variations in the ratios would result in such drastic morphological changes. Another possibility is that the presence of smaller quantities of reacting material in the vicinity of growing $NiMoO_4$ particle nuclei at lower precursor concentrations do not allow the formation of the somewhat larger nanorod structures, while it is possible under higher concentrations of the precursor.

The results from this study also tentatively suggest that a higher degree of crystallinity in the oxide phase results in improved catalytic activity within the final catalysts. However, the crystalline $NiMoO_4$ intermediates undergo a considerable morphological change upon reduction and we do not yet understand the reason for this change.

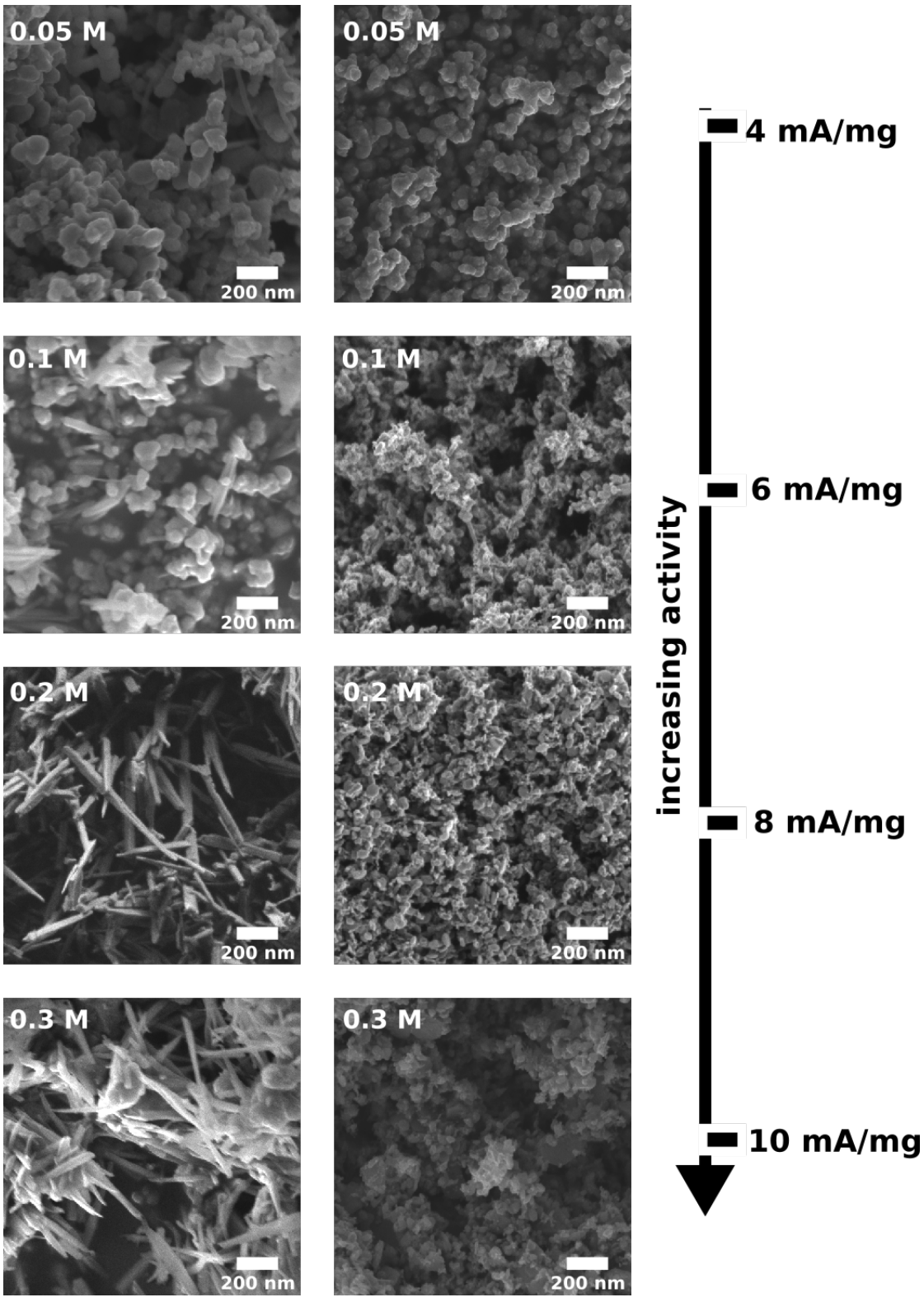

Figure 18: *Representative Scanning Electron Micrographs of (left) $NiMoO_4 \cdot xH_2O$ (right) Ni–Mo systems under increasing molar concentrations of the precursor solutions as marked in the inset. Scale indicating reported activities @ 100 mV overpotentials.*

Next, we evaluated the effect of precipitation time on the HER activity and morphologies of the oxides and catalyst. This was done by a systematic variation of the precipitation timescales while the other synthetic parameters were held constant.This was expected to change the rate of particle growth in the synthesis, where faster heating rates were expected to yield higher supersaturation, resulting in a larger number of $NiMoO_4$ nuclei and therefore smaller particles.

We prepared five samples, synthesized under increasing precipitation timescales ranging from 30sec. to 600 sec. with one at 24 hours. For all samples, we used a precursor concentration of ∼0.125M with Ni/Mo ratios held at 1:1. For samples between 30sec-300sec, the hotplate temperatures for heating were held at 500°C, while for higher time scales the solution was heated at lower temperatures to allow for those time scales without the solution evaporating to dryness. Similar to before, a conscious effort was taken to employ the same techniques during the addition of precursors, precipitate retrieval, and drying and then subsequent reduction.

We observed a wide variability in the catalyst's activity under changing precipitation time scales, as shown in Fig 19. The mass–specific activity indicates nearly a three–fold difference between the least active (300 s) and most active (150 s) precipitation reactions. Surprisingly, though, this variaton did not exhibit any discernible trend with changing precipitation times. This result was curious since the time scales of the growth post–nucleation are expected to be significantly longer with each incrementing time step, of the order of at least 2min for even the smallest time step. Instead, the observed activity followed the order of Ni–Mo @ 300s > Ni–Mo @ 24hours = Ni–Mo @ 30s > Ni–Mo @ 600s > Ni–Mo @ 150s.

The SEM images of the $NiMoO_4$ precipitates and final catalysts corresponding to the reaction time variation are shown in Fig20. The most active and least active systems both exhibit particulate morphologies, while Ni–Mo synthesized using 30 sec. of precipitation time displayed a nanorod morphologies. Nevertheless, the final catalyst displayed particulate morphology in all cases, consistent with the results for variation in precursor concentration. Even if we focus only on relatively fast precipitation reactions, very small changes in reaction time scale (∼1min) clearly lead to drastic changes in catalyst activity. Moreover, these observations subvert our previous conclusion that a more crystalline oxide phase gives a

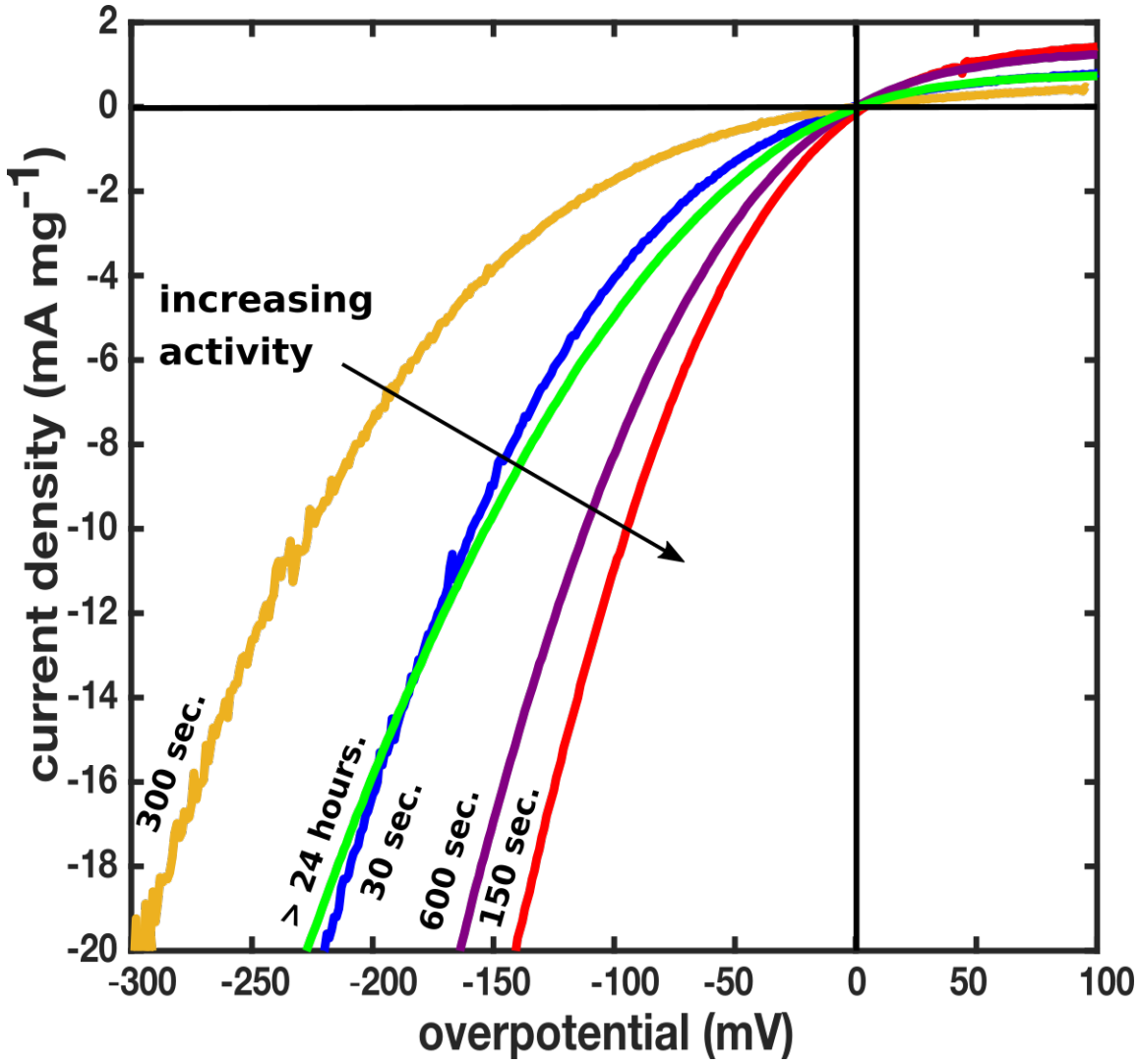

Figure 19: *The comparison of HER catalytic activities from catalysts synthesized from oxides precipitated for different time scales reported as an average of the forward and reverse peaks of the reported catalysts in H_2 saturated 0.1M KOH aqueous solution estimated using electrodes with mass loadings of ∼0.4 mg/cm^2 on Ti substrates. Data was collected using a three electrode cell setup and an Ag/AgCl reference. The contact and solution resistances were compensated using the positive feedback method, with IR resistances ∼20-30 ohms.*

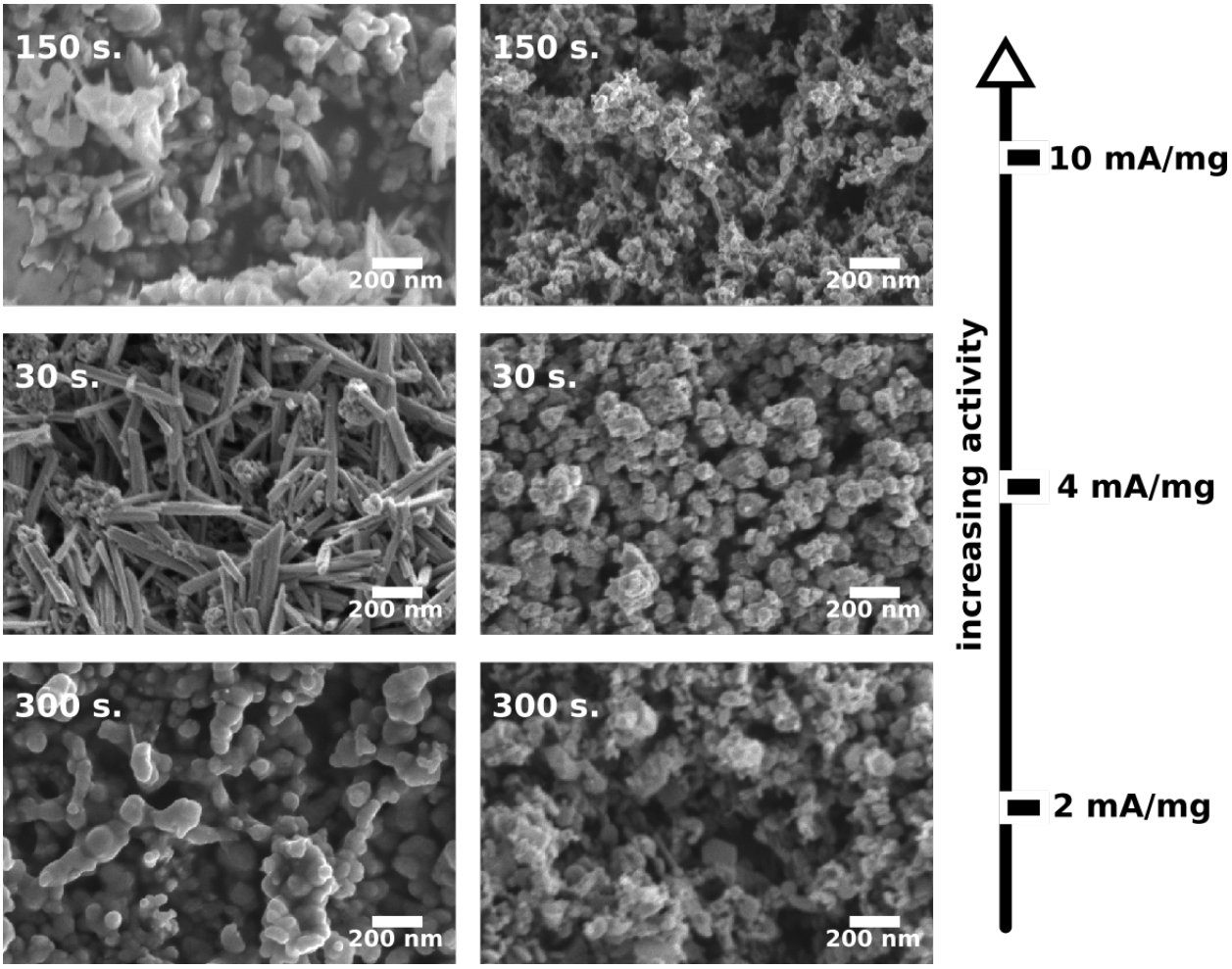

Figure 20: *Representative Scanning Electron Micrographs of (left) $NiMoO_4 \cdot xH_2O$ (right) Ni–Mo systems under different time scales of precipitation for the precursor solutions as marked in the inset arranged in terms of decreasing activity from top to bottom.*

more active Ni–Mo catalyst. Also, there is no intrinsic trend in the morphology change between precipitation time scales and oxide morphologies as had been seen for concentration changes.

It remains largely difficult to ascertain the cause of this variation in the morphology and activity in the intermediate and final phases. It is possible that the use of a batch synthesis that is heated on a hotplate which allows only a uni-directional heating makes it difficult to effectively control solution temperatures evenly. It might be that dead spaces exist within the reaction vessel resulting from non-uniform heating. This would subdue any uniform growth characteristics that might have been possible under increasing time scales of precipitation.This result is a pointer towards the need for a continuous precipitation scheme that might offer a more precise control over the heating rates.

Based on these observations, we are reluctant to make conclusive remarks regarding the effect of precipitation dynamics on the final catalytic activity for Ni–Mo HER catalysts derived from aqueous $NiMoO_4$ precipitation and thermal reduction. It might be so that due to a high degree of change in the system morphology during the reduction, any effect of precipitation parameters on oxide morphology is severely diminished. However, the obvious variation in catalysts activities needs to be further analyzed. It could be arising out of nanoscale structural features that are not visible in an SEM. For example, it may be that there is variation in the thickness of the oxide layer that is forming over the Ni–Mo (see TEM results in Ch2) causes this variation in activity or possibly some other factors that are totally unrelated to the precipitation dynamics. It would be useful to investigate the morphological shift in catalyst morphologies from the intermediate phase to a greater detail, perhaps through the use of in-situ TEM studies of the reduction reaction in order to observe this shift in real-time.

Interestingly, this effect where reduction seems to "converge" the final catalyst morphology would translate into high degree of flexibility during production scale–up, as it would allow for the optimization of precipitation parameters around practical convenience without severely affecting the final catalysts composition, morphology, and activity.

3.3 EFFECT OF REDUCTION DYNAMICS

Since the precipitation dynamics did not exhibit a straightforward effect on the final catalyst activity, we were interested in pursuing activity enhancement by instead varying parameters of the thermal reduction of $NiMoO_4$ to the final Ni–Mo catalyst. Moreover, the results from section 3.2 reflect that reduction, rather than precipitation, may be more important in dictating the final catalyst morphology; this observation demands a better understanding of the effect of the two primary parameters of reduction–time and temperature. As mentioned earlier, we were particularly interested in probing the hypothesis that the concentration of Mo in the final catalyst may be different from the $Ni_{0.9}Mo_{0.1}$ alloy that forms at 450°C if the reduction temperature was varied. The phase diagram for Ni and Mo systems, shown in Fig21, shows that the inter–metallic phase Mo_7Ni_7 is thermodynamically favored at temperatures 500°C and Ni/Mo ratios of unity. We hoped that the use of $NiMoO_4$ as an ordered intermediate oxide of 1:1 ratio of Ni to Mo might be able to form this phase at more modest temperatures than were previously found to be necessary.[86]

On the other hand, it has been noted that during reduction of $NiMoO_4$, Ni^{2+} is first reduced to metallic nickel and only subsequently activates molecular hydrogen, thus enabling complete reduction of Mo^{6+} to metallic Mo within an alloy structure.[97] Based on this formulation, we hypothesized that under thermal reduction conditions, $NiMoO_4$ reacts essentially as a stoichiometric mixture of NiO and MoO_3. Thus the NiO readily reduces to Ni and the MoO_3 to MoO_2, and then the MoO_2 acts as a local reservoir for Mo incorporation into the Ni–Mo alloy. This would suggest that Ni forms first during the reduction and then subsequently there is Mo dissolution on the face–centered sites in the Ni lattice, and the Mo loading in the system may further be constrained by the physical availability of MoO_2 in the near vicinity of Ni particles. Hence, we also conjectured that prolonged reduction of $NiMoO_4$ might also effect a higher degree of Mo dissolution by simply providing more time for solid-state diffusion, thereby resulting in Mo-enriched alloys.

Fig22 shows XRD patterns for powders reduced at 450°C and increasing time scales between 1-16 hours. Mo dissolution into Ni results in a leftward peak shift indication an expansion of the Ni lattice. However, the Ni fcc peaks do not exhibit increasing shifts even

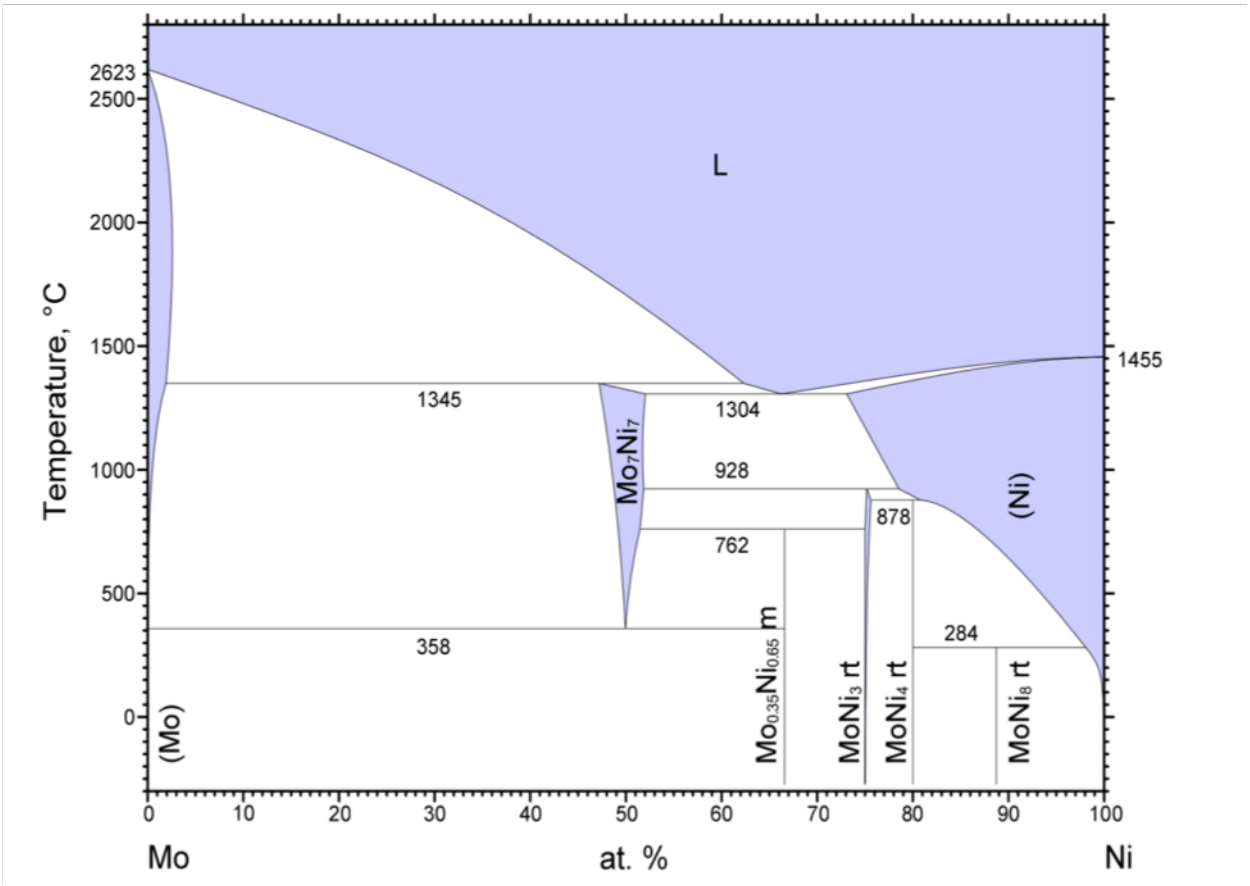

Figure 21: *Phase diagram for Ni–Mo systems.*[113]

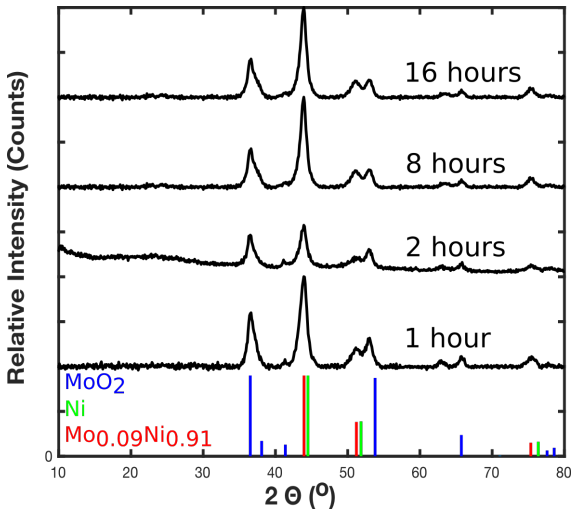

Figure 22: *Representative X-ray diffraction data for the final catalysts synthesized via reduction at increasing time scales along with standard peaks for Ni and MoO_2.*

at reaction timescales as long as 16 hours. This indicates that the $NiMoO_4$ reduction to Ni–Mo and MoO_2 is tentatively complete within the first hour. Thus, we conclude that it is not practically possible to dissolve more Mo in the Ni lattice under these conditions, either due to the limited local availability of Mo or another effect that we have not yet considered. Since the chemical composition of the catalysts prepared at higher time scales is the same, any activity improvement over that achieved by a typical reduction process is unlikely, and in fact, lower activities are likely with prolonged heating due to particle sintering.

In further experiments intended to understand the effect of reduction temperatures on the structure and composition of the Ni–Mo composites, we reduced the $NiMoO_4$ intermediates at increasing temperatures between 300°C and 1000°C. Fig 23 presents the XRD data for powders reduced under these varying temperatures. The reaction was expected to begin around 300°C, and indeed the XRD data for thermally treated powders show the emergence of Ni or MoO_2 only as the temperature is increased from 300 to 500 °C. Beginning at 500°C, the predominant phases are Ni and MoO_2 along with an additional complex Ni–Mo oxide phase as a minor product. At still higher temperatures, the reaction tends to drive the reduction all the way to metallic Mo, along with Ni–Mo alloy and residual MoO_2. This lends

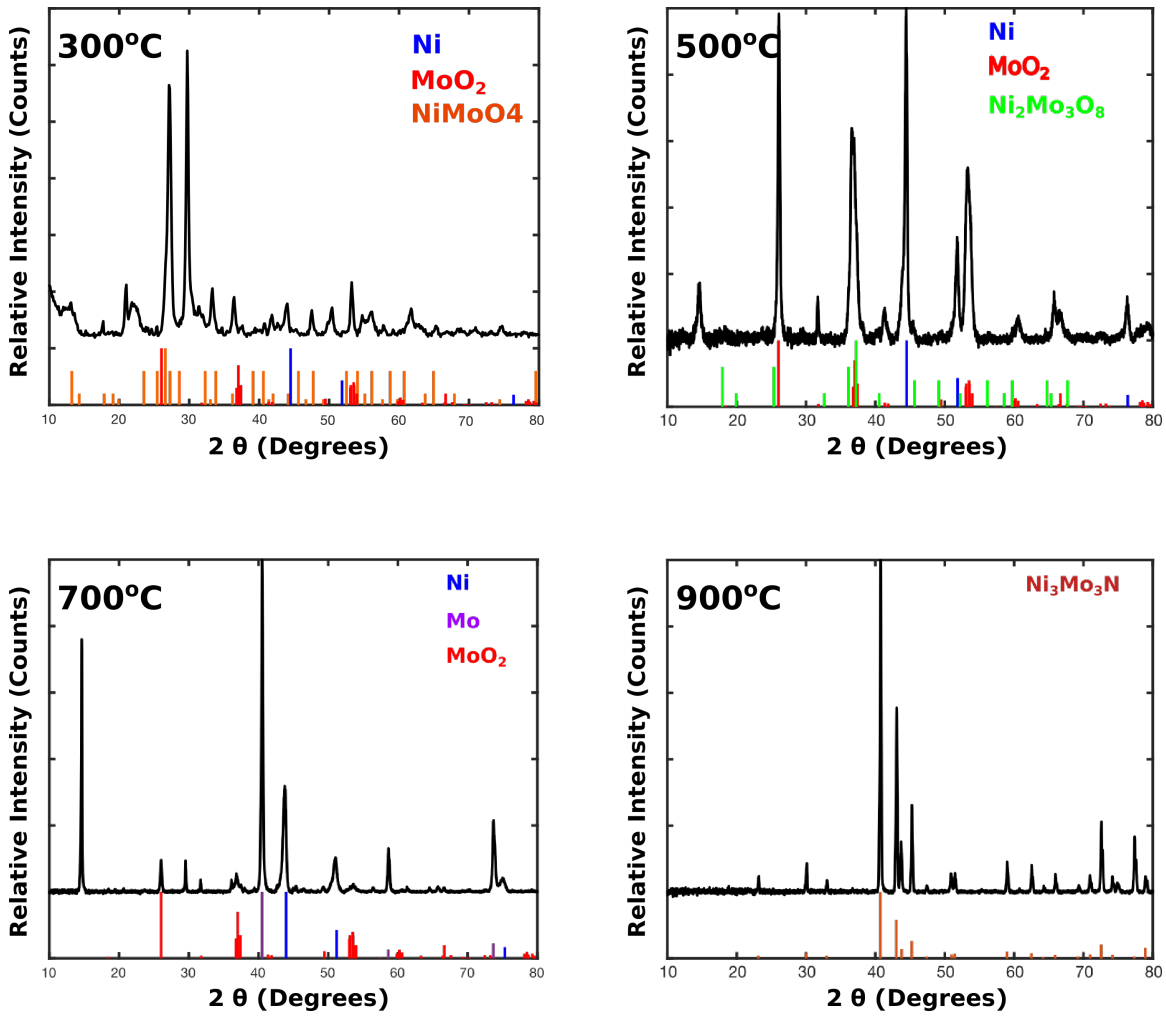

Figure 23: *Representative X-ray diffraction data for the final catalysts synthesized via reduction at increasing temperatures between 300°C and 900°C along with standard peaks for the primary products signified in different colors in the inset..*

some support to our theory that the Ni in the system reduces first, activating the molecular hydrogen to drive the reduction of Mo^{6+}, since much higher temperatures and longer reaction times are required for direct formation of Mo from MoO_3 and H_2.[97] Interestingly, at a temperature of 900°C, we observed near quantitative formation of Ni_3Mo_3N, which can be ascribed to the activation of N_2 in the forming gas atmosphere used for this reaction (5 wt% H_2, 95% N_2). This nitridation reaction was also observed by Csernica et al.[86] We concluded this line of study at temperatures below 1000°C due to limitations of safe operation on our furnaces along with the formation of nitrides, which are not the focus of this work. However, even if the desired Mo_7Ni_7 does form around these temperatures, it would certainly sinter severely into large particles, as observed by Csernica and McKone during their attempts synthesize this inter-metallic from an ammoniacal precipitation reaction. Hence, it would not be possible to resolve the ambiguity surrounding the effect of structuring and bulk enrichment of Molybdenum in the Ni–Mo catalysts.[86]

3.4 EFFECT OF RUTHENIUM DOPING IN NI–MO

Hydrogen evolution/oxidation catalytic activity is strongly dependent on the adsorption /desorption energy of hydrogen on the catalyst surfaces. In aqueous acid media, the H_2 adsorption process is arguably straightforward since it proceeds from electron transfer coupled with protons discharge from H_3O^+ cations to yield water, which is simply the bulk solvent. However, in alkaline media H_2 adsorbs through coupled electron transfer and H_2 discharge from water itself and resulting hydroxide as the product, whose interactions with the catalyst surface may be stronger or more complex than water.[114,115] Thus even Pt HER electrocatalysis is considerably slower in aqueous base than in acid conditions.[116] Subbaraman et al. developed hetero-structured $Pt/Ni(OH)_2$ catalysts that "recovered" the HER activity of Pt in base to near the same level as observed in acid.[115] These researchers argued that the $Ni(OH)_2$ improved the water dissociation kinetics at the metal/hydroxide interface, thereby increasing the overall reaction rate. The same approach was used by Gong et al. to design nanoscale NiO/Ni heterostructures that enhanced the activity of Ni for HER.[107]

Zheng et al. synthesized anomalously structured $Ru/C_3N_4/C$ catalysts that exhibited better geometric activities than benchmark Pt/C catalysts towards the HER, and they used DFT computations to suggest that the low water-dissociation barrier of Ru as compared to Pt was behind the high activities observed from these systems.[117] Based on these prior results, we postulated that we could enhance the activity of Ni–Mo catalysts by generating Ni–Mo/Ru heterostructures via Ru doping through incipient wet impregnation. This straightforward approach is popular in gas-phase catalyst design and has also been used in some measure for synthesizing active electrocatalysts.[118–120]

We used an aqueous $RuCl_3$ solution for impregnation of dehydrated $NiMoO_4$ We first prepared an aqueous solution of $RuCl_3$ of appropriate concentration such that the wetting of $NiMoO_4$ powders with the aqueous $RuCl_3$ would result in a predefined mixture of Ru:(Ni+Mo) in the mixture ($\sim$ 1-5% Ru/(Ni+Mo)). This $RuCl_3/NiMoO_4$ mixture was calcined in air to oxidize the Ru salt to RuO_2 before finally reducing the mixture in H_2 atmosphere under conditions otherwise identical to our pure Ni–Mo reduction. We first synthesized these catalysts with 1 mol% Ru dopant on a total metal basis, and later increased the doping level to 5 mol% Ru. EDS mapping of a Ni–Mo–Ru containing 5 mol% Ru is shown in Fig 24, and confirms a homogeneous dispersion of Ru on a submicron scale.

Representative alkaline HER current vs. potential data for Ni–Mo–Ru catalysts containing 0(typical Ni–Mo), 1 and 5 mol% Ru are illustrated in Fig25, along with an additional control comprising pure Ru catalyst supported on carbon containing the same mass of Ru in the system as in the 1 mol% Ni–Mo–Ru catalyst. The HER characteristics of these systems show a monotonic increase in activity with increasing amount of Ru doping. However, the Ru/C catalyst alone exhibits comparable activity to pure Ni–Mo even though it contains only $\sim$1/100 as much total catalyst mass. Thus, the observed activity increase at 1 and 5 mol% Ru loadings in Ni–Mo–Ru can essentially be accounted for by invoking a linear combination of the activities of Ni–Mo and Ru alone. Thus, we conclude that Ru does not synergistically enhance the activity of Ni–Mo in excess of the enhancement that Mo provides alone. More broadly, we conclude that Ru-doped Ni–Mo heterostructures derived from incipient wet impregnation are not any more attractive than Ni–Mo (moderately active and cost-effective) or Ru (highly active but costly) alone for alkaline electrolyzer cathodes.

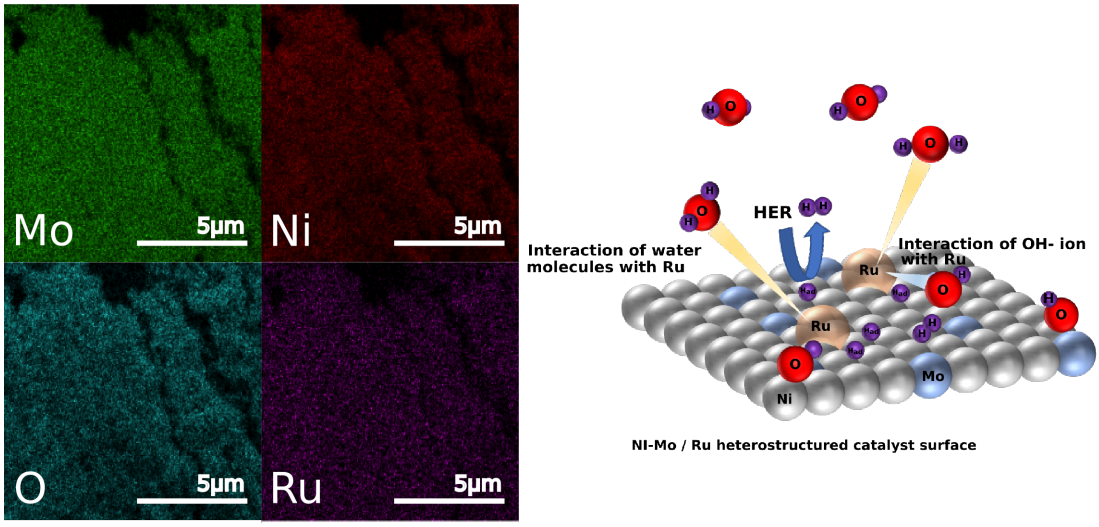

Figure 24: *(left) EDS elemental maps of Ni–Mo/Ru catalyst systems synthesized via incipient wet impregnation post reduction illustrating a homogeneous dispersion of Ru within the final Ni–Mo/Ru catalyst body (right) Illustration of expected surface interactions of Ni–Mo/Ru and Ru in an alkaline media*

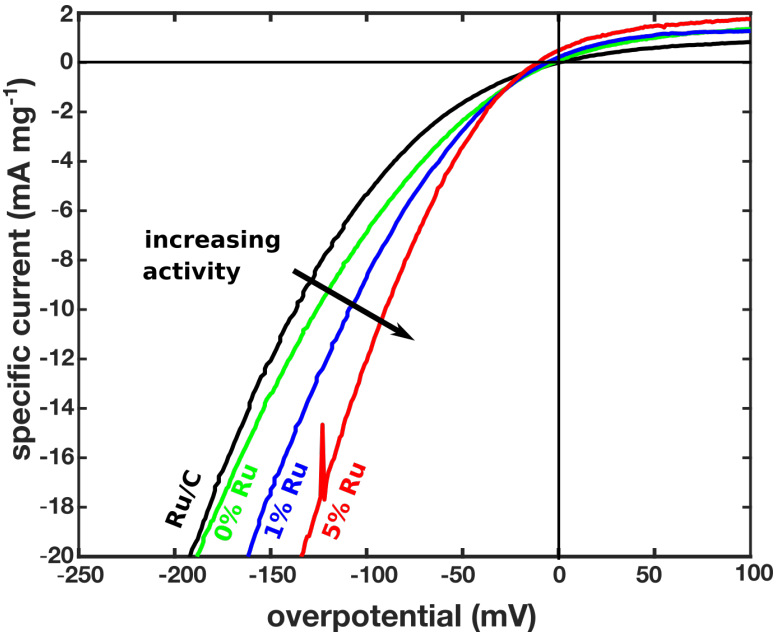

Figure 25: *The comparison of HER catalytic activities from Ni–Mo/Ru heterostructured catalysts with increasing amounts of Ru dopant in the system reported as an average of the forward and reverse peaks of the catalysts in H_2 saturated 0.1M KOH aqueous solution estimated using electrodes with mass loadings of ∼0.4 mg/cm^2 on Ti substrates. Data was collected using a three electrode cell setup and an Ag/AgCl reference. The contact and solution resistances were compensated using the positive feedback method, with IR resistances ∼20-30 ohms.*[115]

3.5 EFFECT OF SYNTHESIZING CARBONACEOUS HYBRIDS FOR NI–MO

As noted in Ch2, the HER behavior of Ni–Mo systems deviate from typical Tafel behavior at high overpotentials. This characteristic of Ni–Mo systems was further illustrated by plotting the current vs potential HER data of Ni–Mo and Pt as a tafel plot in Fig26, placing *log(j)* on the absicca and η on the ordinate. Under kinetic control, the HER data for these systems ought to exhibit exponential behavior in the Tafel region ($>$ 100mV) i.e a linear curve above $\eta >$ 100mV. A linear best fit was generated for each curves within the tafel region, plotting residuals as a function of overpotential range in each. As demonstrated by the residual data in the inset box in Fig26, the HER curves for Pt exhibits more–or–less linear behavior above 100mV while the Ni–Mo HER curves demonstrate significant deviations from the linear behavior based on the aforementioned best fit.The higher slope of the Ni–Mo systems as compared to the Pt behavior also indicate that the Ni–Mo systems are likely to exhibit transport limitations at lower current densities than Pt, another indicator of the presence of activation barriers other than kinetics. Lastly, the Tafel plot also shows that Ni–Mo systems cannot be described appropriately by Tafel law at low overpotentials, possibly due to significant back reactions.

The deviation of HER activity of Ni–Mo systems from typical Tafel behavior at high overpotentials is hypothesized to arise due to a high inter-particulate resistance within the catalysts which results in increased voltage drop at higher current densities resulting in a lower observed activity of the system. (see Fig13) Because these effects are not attributable to intrinsic catalytic activity, they convolute proper characterization of composition-structure-function relationships in this catalyst. There exist a number of reports that leverage the high conductivity of graphitic carbon materials to enhance the electrical conductivity of the catalyst systems. One recent example involves the use of carbon blacks as supports for MoSx catalysts, which are active HER catalysts in acid but suffer from very low conductivity.[111]

A wide range of graphitic carbon additives can be used as conductivity enhancers in electrocatalyst materials, including vulcan carbon, carbon nanotubes, graphene, or graphene oxides. In ongoing work in the McKone lab, Rituja Patil has found that Ni–Mo catalysts

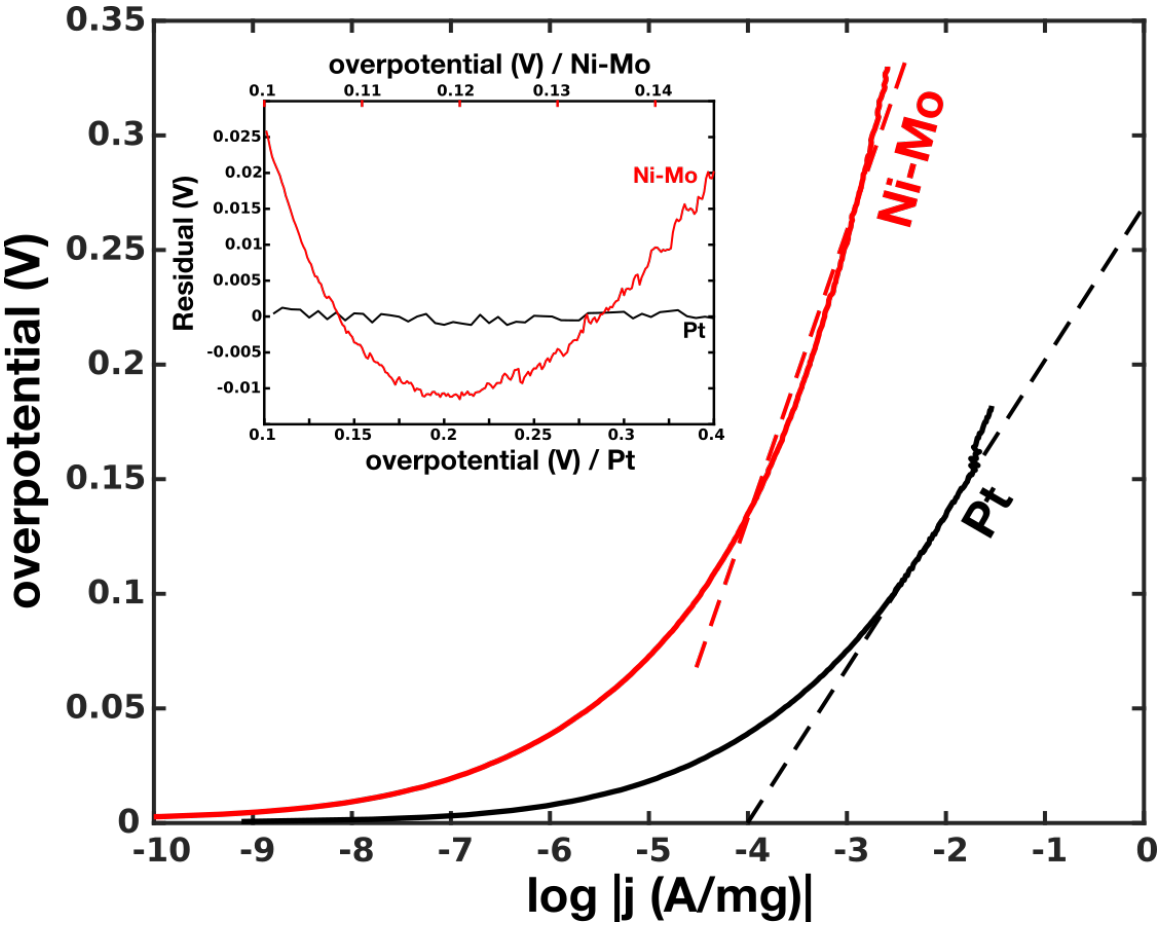

Figure 26: Tafel plots of Ni–Mo along with a Pt control reported as a η - *log(j)* curve meant to illustrate the deviation of Ni–Mo HER data from typical Tafel behavior. The straight dashed lines along with each curve represent the linear best fit of the Tafel data for Ni–Mo and Pt at $\eta > 100$mV. The residuals from each fit are plotted in the inset box as a measure of the degree of deviation from Tafel law

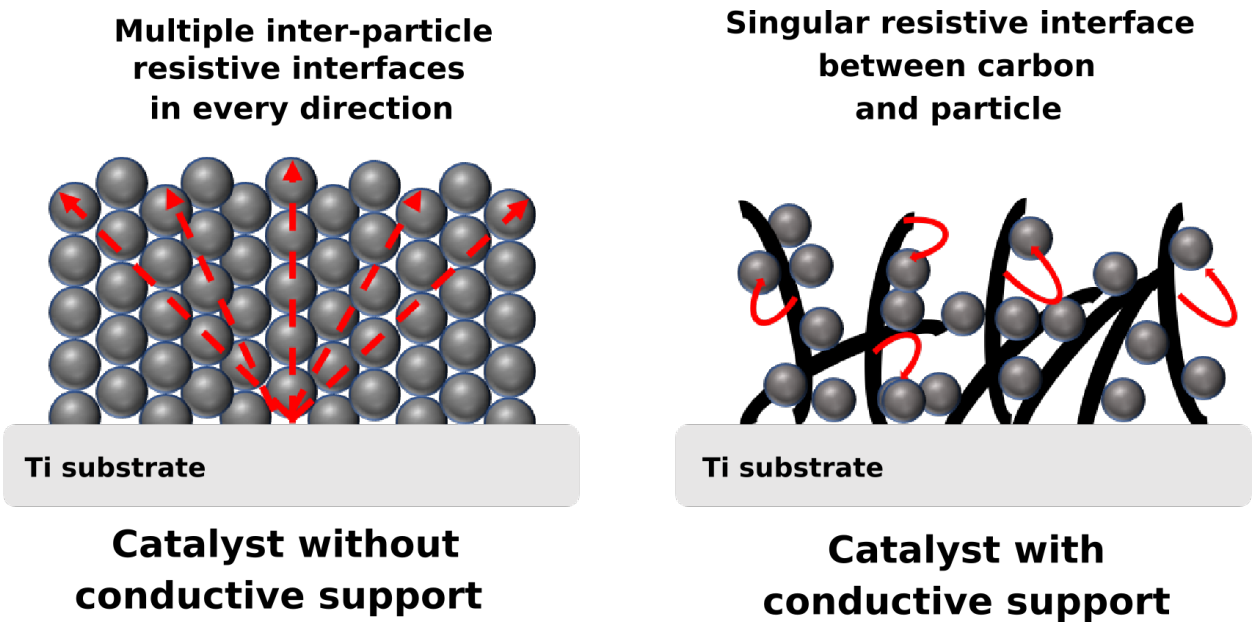

Figure 27: *Illustration of the (left) multiple resistive inter-particle interfaces in a typical Ni–Mo system without conductive support.(right) reduction in number of resistive inter-particle interfaces in Ni–Mo systems with conductive carbon supports*

composited with Vulcan carbon blacks exhibit markedly improved HER performance, which we attribute to the availability of efficient electron transport channels within the catalyst mass, made possible by the presence of carbon in the catalyst mass. Carbon additives may further enhance Ni–Mo catalytic activity by improving dispersion of the catalyst particles throughout a porous and conductive carbon matrix. The enhancement of electronic transport in the catalyst system through the presence of conductive supports is illustrated in Fig27

We call our preferred approach for carbon incorporation the "paste method", wherein a known quantity of vulcan carbon is added to the intermediate oxide and ground by hand with a mortar and pestle in the presence of isopropanol to make a paste. The solvent is then dried in an oven and the dry composite is subjected to a typical reduction step. Crucially, the use of carbon substrates eliminate the need for a second reduction/activation step for these systems and hence is useful not only to enhance the activity of the system but also the processability of the synthetic approach. It has already been observed that the electrical conductivity issue is dominant in Ni–Mo systems synthesized via the ammonia-free

synthesis as seen in Fig26 Hence, we conjectured that carbon incorporation would result in comparable, if not greater, improvements in observed catalytic activity. Fig29 shows the characteristic HER performances of the Ni–Mo systems with and without an activating anneal as compared to the best performing Ni–Mo/carbon hybrid catalysts as well as Pt benchmark. The Ni–Mo/carbon catalyst indeed show a marked increase in activity relative to all other samples derived from $NiMoO_4$ precipitates. Note that arguably the most relevant comparison is between Ni–Mo/C catalysts and pure Ni–Mo without an activating post-anneal step, as these films underwent identical processing except for the step in which carbon was composited with the oxide. As noted in Ch-2 the "extra" post-annealing step was required in order to gently sinter the particles to the Ti substrate as well as each other in order to overcome adhesivity and conductivity issues within the system.

Carbon is a conductive material and as such, its use as a support eliminates the need for the post-anneal activation step. In this context, Ni–Mo/C displays nearly forty-fold higher activity at 100mV overpotential as compared to Ni–Mo systems that do not undergo the annealing step. Remarkably, the Ni–Mo/C systems also exhibits almost a three fold activity rise as compared to the previously Ni–Mo systems undergoing activation even though there is less catalyst mass present. This is attributed to the higher degree of dispersion possible in Ni–Mo systems annealed with carbon support as well as the provision of efficient electron channels within the catalyst mass by carbon (see Fig28) as compared to those achieved through simple particle sintering which implicitly reduces active surface areas in the catalyst.

The significant activity enhancement qualitatively illustrates the importance of inter-particle electrical resistance as a major limitation in these catalysts. The use of carbon is common in modern PEM-based fuel cell configurations as a porous, conductive matrix for efficient utilization of the electrocatalyst.[84,85] This strongly supports our aim of creating highly processable systems that can be integrated into the mainstream using prevalent techniques. Thus, we strongly favor carbon incorporation over post annealing as the most effective way to mitigate conductivity limitations in these systems.

We hypothesize that further improvements in Ni–Mo/C HER catalyst performance can be made by further optimizing the carbon compositing step, and we have made some preliminary efforts toward this optimization. We hypothesized that the use of excessive carbon will result

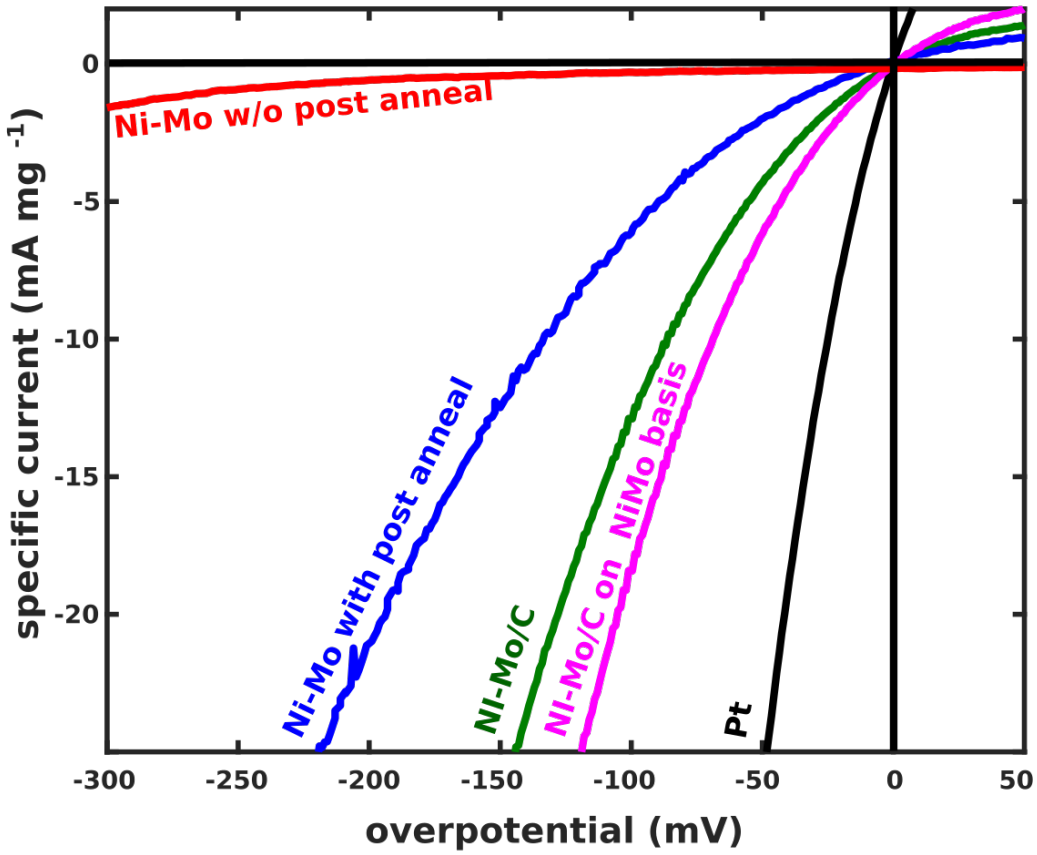

Figure 28: *The comparison of HER catalytic activities from the different Ni–Mo systems with and without carbon along with a Pt control reported as an average of the forward and reverse peaks of the catalysts in H_2 saturated 0.1M KOH aqueous solution estimated using electrodes with mass loadings of ∼0.4 mg/cm^2 on Ti substrates. Data was collected using a three electrode cell setup and an Ag/AgCl reference. The contact and solution resistances were compensated using the positive feedback method, with IR resistances ∼20-30 ohms. The "Ni–Mo w/o post anneal" refers to Ni–Mo nanopowders that did not undergo a post annealing "activation step" prior to testing. Ni–Mo with post anneal is the analogous system that did undergo this activation step."Ni–Mo/C" refers to a hybrid Ni–Mo and carbon system containing a 30% mass ratio of carbon to catalyst."Pt" refers to the Pt control catalyst developed using methods developed by other researchers internally in the lab.*

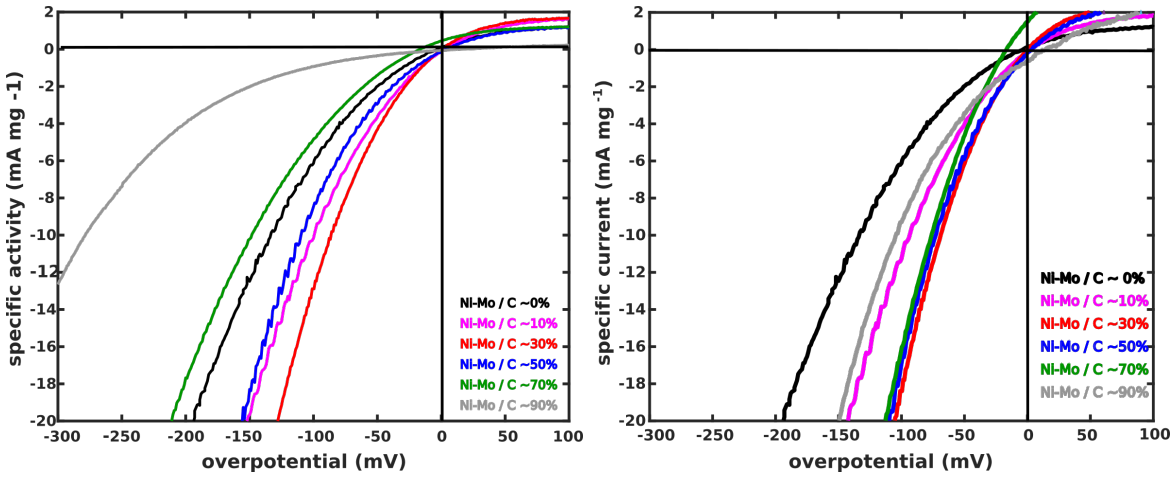

Figure 29: *The HER performances of Ni–Mo / Carbon systems at increasing mass ratios of carbon in Ni–Mo normalized to (left) total catalyst mass of Ni–Mo + Carbon and (right) total mass of Ni–Mo only reported as an average of the forward and reverse peaks of the catalysts in H_2 saturated 0.1M KOH aqueous solution estimated using electrodes with mass loadings of ∼0.4 mg cm^2 on Ti substrates. Data was collected using a three electrode cell setup and an Ag/AgCl reference. The contact and solution resistances were compensated using the positive feedback method, with IR resistances ∼20-30 ohms.*

in diminishing improvements in electronic conductivity and will being to impose transport limitations. Therefore, we attempted to identify the ideal mass ratios of Ni–Mo to carbon that should be maintained to yield the highest performance. Fig29 shows the HER activity at increasing carbon loadings, as normalized to both total catalyst mass (Ni–Mo + carbon) and Ni–Mo mass alone. Activity on a total catalyst basis clearly peaks at a relatively modest 30 wt% carbon loading; activity normalized to Ni–Mo mass only also reaches a maximum at 30 wt% carbon loading, but remains high up to 70 wt% carbon. The Ni–Mo/Carbon with 90% mass ratio of carbon in the total catalyst shows a significant depreciation in activity, which agrees with the conclusion that excessive carbon yields transport limitations.

In considering further work on Ni–Mo/carbon catalyst synthesis and characterization, it would be interesting to pursue studies of various carbon additives in the interest of identifying the most effective conductivity promoter. The optimum mass ratios of carbon to metal would ultimately depend on the morphology and aspect ratio of the carbon materials as well as the degree of dispersion of the catalyst and carbon. In any case, we broadly conclude that the

carbon additives mitigate the conductivity limitations prevalent in Ni–Mo HER catalysts, thereby allowing them to exhibit practical performance that more closely reflects its intrinsic activity.

3.6 CONCLUSION

To summarize, we evaluated the significance of some of the precipitation and reduction parameters during synthesis of Ni–Mo nanopowder catalysts. We tentatively concluded that it is difficult to quantitatively link the precipitation dynamics to the final HER activity of the catalysts, mainly due to the drastic change in system morphologies during reduction, especially for crystalline nanorod $NiMoO_4$ such that any effect of precipitation would become severely diminished. We also found that reduction timescales as long as 16 hours do not have any appreciable effect on overall Ni–Mo catalyst composition, and changing the temperatures of reduction results in formation of Mo metal and eventually Ni–Mo nitrides (in N_2 environments) rather than Mo-enriched Ni–Mo composites.

Further, we demonstrated that Ru doped Ni–Mo heterostructures derived via incipient wet impregnation do not offer any synergistic enhancement of the activity of Ni–Mo. Hence, they are not more attractive than pure N–Mo systems since Ru is a highly costly precious metal. Lastly, we found that compositing carbon with Ni–Mo nanopowders results in greatly enhanced HER activity due to improved electronic conductivity, and 30 wt% Vulcan carbon loading yields optimum activity for Ni–Mo derived from $NiMoO_4$.

Going ahead, it will be important to identify the underlying synthetic parameter or parameters that gives rise to widely variable Ni–Mo catalyst activities. This could possibly be achieved via in–situ TEM studies wherein we can directly observe changes in catalyst morphology upon reduction in real time. It would also be worthwhile to better quantify the inter-particle electrical resistances that otherwise limit Ni–Mo activity. Electrochemical impedance spectroscopy measurements could perhaps be employed to good effect. Both of these advances would ultimately support the design of better Ni–Mo/carbon catalysts en route to efficient alkaline water electrolyzers.

4.0 EXPERIMENTAL AND MATERIAL SYNTHESIS

This chapter seeks to expand on the specific experimental and material synthesis techniques that were learned and developed during the course of this work. I have tried to include the description of each technique employed in adequate detail for someone with a modest background in chemical synthesis to reproduce and hopefully expand on the above work. It starts with an elaboration of the synthesis method for each type of catalysts developed for the work. Most of these techniques are adapted from the prior synthesis of similar material as noted in the main text. The electrochemical and physical characterization techniques that follow are typical in electrochemistry and have been provided to lend perspective on the results derived from these tests. The sample preparation for each of these studies has been included as a tutorial support to describe the best practices to follow when pursuing these tests as I have come to learn during the course of my work.

4.1 CATALYST SYNTHESIS

The catalyst synthesis described here is representative of a typical procedure followed for generation of Ni–Mo nanopowder catalysts from $NiMoO_4$ powders using an aqueous precipitation reaction followed by thermal reduction, as illustrated conceptually in Fig. 30. During the course of this work, a range of synthetic variables were individually varied as needed for each study. Thus, the synthesis and processing methods that were used throughout this work followed the procedure described here, unless otherwise noted. All reagents were purchased from commercial sources and in analytical or reagent grade when possible. All water used was purified using a Millipore Nanopure water purification system (18.2 MΩcm resistivity).

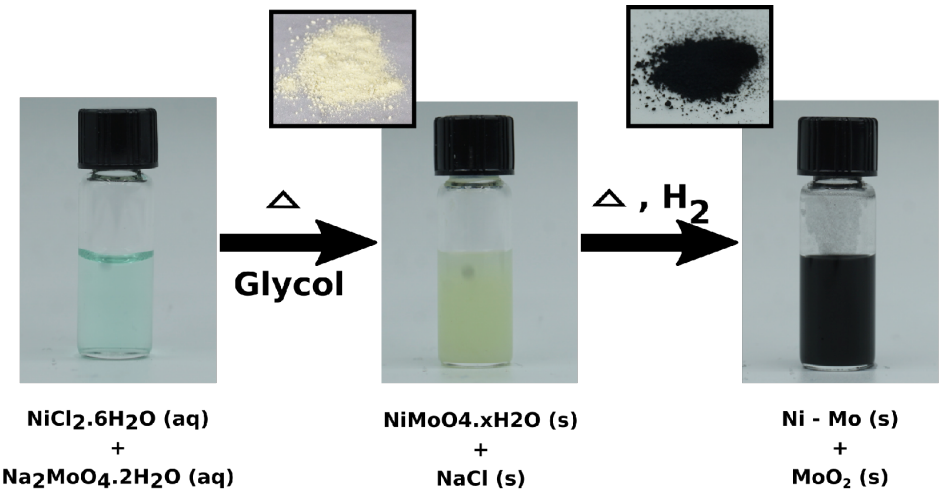

Figure 30: *Synthetic scheme for Ni–Mo nanopowders consisting of precipitation of $NiMoO_4$ from an aqueous solution of $NiCl_2$ and Na_2MoO_4 followed by thermal reduction under a H_2 atmosphere along with the dry powder of oxides and final catalysts as formed during a typical synthesis*

4.1.1 Synthesis of "Ammonia-Free" Ni–Mo Nanopowder

First, an aqueous solution was prepared containing 0.75g of $NiCl_2 \cdot 6\,H_2O$ (Alfa Aesar, 99.3%) and 0.75g of $Na_2MoO_4 \cdot 2\,H_2O$ (Alfa Aesar, 99.5%) in 25mL deionized water, yielding a clear green solution. The solution was either prepared in or transferred to a 500ml borosilicate beaker. A hotplate was then preheated to 500°C, and once the hotplate temperature became stable, 25ml diethylene glycol (Alfa Aesar, 99%) was added to the green aqueous solution and the entire mixture was set on the hotplate with stirring set to 750RPM using a teflon–coated magnetic stirrer. The solution became increasingly opaque as it was heated, which indicated the progression of the precipitation reaction. The colloidal mixture was allowed to heat for ∼2 min, after which it was immediately transferred to an ice bath to quench the reaction by bringing down the temperature.

The solution was allowed to stand in the ice bath for ∼2 min before transferring it to a 50ml centrifugation tube. The suspension was then centrifuged at 3000 RPM for 10 min to separate out the precipitate. After centrifugation, the tube contained a yellowish–green precipitate at the bottom along with a clear green supernatant. The supernatant

was discarded and the precipitate was washed with 5 ml of water. The precipitate was then agitated and subsequently sonicated for 5 min to ensure thorough mixing with clean water. This again formed a suspension, which was centrifuged for a second time in the same way as before. The centrifugation yielded a reduced quantity of precipitate and a clear green supernatant. Although it might be useful to perform more water washes, due to the solubility of the precipitate in water, additional washes were found to reduce the precipitate yield to insufficiently low amounts. A subsequent wash of the remaining precipitate was then carried out using acetone instead of water, and it resulted in minimal decrease in the amount of precipitate and a clear transparent supernatant that was again discarded. Finally, the precipitate was suspended in a small amount $\sim$ 5ml of methanol before being transferred to a petridish. The precipitate was then placed in an oven set 60°C for several hours to evaporate out the methanol. The final product was a fine, flowing greenish-yellow powder of hydrated $NiMoO_4$. The final oxide yield based on mass of precipitated oxide upon total mass of precursor metal was found to typically range $\sim$30%.

These greenish–yellow oxide powders were then placed in a quartz glass crucible and heated in a Thermo Scientific Lindberg/Blue M "Mini Mite" Tube Furnace set to 450°C for 1 hour under forming gas (5% H2, 95% N2, Matheson) flow in the tube. After heating, the gas flow was switched off and the black solids were allowed to cool in the furnace to room temperature. Once cooled, the reaction tube was unsealed and the crucible was allowed to remain in the furnace for 15 min before being retrieved from the one end of the tube. We believe that cooling and standing in the air allows for slower oxidation of the active catalyst surface, whereas rapid removal to air sometime yields pyrophoric reactivity.

The final catalyst powders were stored in glass vials. These powders were subsequently suspended in isopropanol (Aldrich) using a bath sonicator for 30 minutes to yield a black colloid. The black colloid remained well suspended for only a few minutes and needed to be agitated or sonicated again prior to use.

4.1.2 Synthesis of Ni–Mo/Ru heterostructure synthesis

The dry, yellow-green oxide powders of $NiMoO_4 \cdot xH_2O$ were prepared as described in subsection 4.1.1. These oxide powders were dehydrated by heating for 1 hour in a Thermo Scientific Lindberg/Blue M Moldatherm Box Furnaces set to 400°C. After an hour, the powders were allowed to cool to room temperature while still inside the furnace. A pale brown powder was retrieved and weighed using a micro-balance. The dehydration resulted in a 7-10% reduction in the oxide weight.

The dehydrated $NiMoO_4$ powder was doped with Ru by an incipient wet impregnation technique.In order to prepare a 1% Ru doped Ni–Mo system, an aqueous solution of 0.0475g $RuCl_3$ was prepared in 5ml water, such that mixing with the desired quantity of $NiMoO_4$ powder would yield the desired mole ratio of Ru to total metal content. 0.1g of the dehydrated oxide powder was ground using a mortar and pestle, loaded into a quartz glass crucible, and wetted evenly by 100µL of the aq.$RuCl_3$ solution prepared earlier using a micro pipette. This crucible was then loaded onto a flow furnace and heated in open air at 400°C for 1 hour in order to convert the $RuCl_3$ to RuO_2. Then the reaction tube was sealed and the powders reduced at 450°C for 1 hour under the flow of forming gas. The catalyst powders were retrieved after cooling and processed into colloidal inks as described in subsection 4.1.1.

We can use the same methodology to prepare Ni–Mo/Ru systems with different amount of Ru dopings – 1%, 2% or 5%. This is done by changing the concentration of the $RuCl_3$ doping solution appropriate to the required loading prior to the wetting of the oxides.

4.1.3 Synthesis of Ru/carbon mixtures

Similar to synthesis described in section 4.1.2, Ru/C control catalysts was prepared via incipient wet impregnation of Ru on oxidized carbon. The Vulcan carbon XC–C72 was oxidized using H_2O_2 as described by Malek et al. by agitating the solution of carbon black and H_2O_2 at 700 RPM and 60°C on a hotplate for over 24hours.[121] The mixture was then poured into a centrifugation flask and washed with an excess of distilled water and then purified by centrifugation at 3000RPM for 10 min to separate out the carbon black and water-H_2O_2 supernatant. The supernatant was subsequently discarded and the carbon black

was re-agitated in water. This washing step was repeated two more times to ensure that all H_2O_2 in the system has been removed. Finally, the carbon black was suspended in distilled water again and emptied out into a petridish. The petridish was heated at 60°C in the oven to dry out the carbon black and yield dry oxidized carbon black powders.

First, the mass reduction of $NiMoO_4$ during the dehydration phase was estimated via thermogravimetric analysis(TGA), amounting to ∼30%. Then the black powders prepared earlier were used for the Ru impregnation in synthesis of Ru/C using the same incipient wet impregnation technique discussed in section4.1.2. In order to prepare a 1% Ru/C system, carbon of mass equivalence to the reduced catalyst mass (see section4.1.2 was taken in a quartz glass crucible i.e 0.1g Carbon. It was wetted using 100µL of the aq.$RuCl_3$ solution prepared earlier in section4.1.2 with the help of a micro pipette. This will in turn ensure that equivalent quantities of Ru end up in the Ru/C and Ni–Mo–Ru systems when they are deposited on foils to make the electrodes. This system is allowed to go through the same oxidation-heating process described in section4.1.2 to prepare the final Ru/C catalysts. These catalysts were then recovered after cooling and made into colloidal inks.

4.1.4 Synthesis of Ni–Mo/Carbon hybrid structures

The dry, yellowish–green oxide powders of $NiMoO_4 \cdot xH_2O$ were prepared in the same manner as sectionsynNiMo. The expected mass reduction for $NiMoO_4 \cdot xH_2O$ during the reduction step was estimated via thermogravimmetric analysis(TGA) studies as ∼30% . It should be noted here that there was no mass reduction of carbon black during the reduction phase. Hence, the mass of carbon black needed in the final catalyst (dependent on mass ratios) was added to dry greenish-yellow powders of the oxide in the form of Vulcan carbon XC–C72. The mixture of carbon black and oxide powders were put in a mortar-pestle and a minimal amount of isopropanol that is just enough to wet the mixture is added to it. This mixture was then homogeneously dispersed using the pestle resulting in a black paste. This system is heated in an oven set to 60°C for an hour to dry out the paste.

These mixed powders were then transferred to a borosilicate crucible and heated in a Thermo Scientific Lindberg/Blue M "Mini–Mite" Tube Furnace set to 550°C for 1 hour under

forming gas (5% H2, 95% N2, Matheson) flow in the tube. After heating, the gas flow was switched off and the black solids were allowed to cool in the furnace to room temperature. Once cooled, the reaction tube was unsealed and the crucible was allowed to sit in the furnace for 15min before being retrieved from the one end of the tube. The active catalysts so formed was in powder form. It can then be stored in a glass vial as it is or made into colloidal inks using isopropanol.

4.1.5 Synthesis of Pt/Carbon benchmark catalysts

Pt nanoparticles were synthesized using a one-pot reaction developed previously in the McKone lab by Dean Miller. A total of 10mL of the aqueous solution was made containing 1mM H_2PtCl_6, 1mM $(C_3H_3NaO_2)$n, and 10mM $C_6H_8O_6$. The solution was stirred and brought to boil for 1 hour, with water being added to replace the boiled-off water. The solution was removed from heat, and one pellet of NaOH was added to the solution and was allowed to sit overnight. After settling, clear evidence of precipitation was seen. The solution was then centrifuged three times at 15000 RPM, replacing excess water with fresh water between each cycle. After the final washing cycle, the purified aqueous nanoparticles were dried in a drying oven set to 60°C and a known amount of water was added to the dry nanoparticles.

4.2 PHYSICAL AND COMPOSITIONAL CHARACTERIZATION

4.2.1 X-Ray Diffraction Spectroscopy (XRD)

XRD spectra were collected on both the intermediate oxides as well as the final reduced catalyst for identification using a Bruker D8 DISCOVER X-Ray Diffractometer (XRD)with Cu K radiation(Kα1, λ= 1.5406Åand Kα2, λ= 1.5444 Å). The measurements were carried out on closely packed powders that had been ground with a mortar and pestle to break down large agglomerates and supported on a clean glass slide. The XRD data was used for matches against standard powder diffraction patterns using Brukers DIFFRAC.EVA phase analysis software.

4.2.2 Scanning Electron Microscopy (SEM) and Energy Dispersive Spectroscopy (EDS)

The morphology of the intermediate phase and final catalyst powders were characterized using scanning electron microscopy on a JEOL JSM-6510LV/LGS Scanning Electron Microscope (SEM) with Oxford Inca equipped with an inbuilt EDS system. The imaging was done on oxide and catalyst inks coated on Ti foils at magnifications ranging from 100X – 200,000X and at low accelerating voltages of 1-3 kV due to the prevalence of charging effects. Images for the EDS mapping were captured at a minimum 10kV accelerating voltages. The images produced from SEM and EDS data were subjected to a minimum of post-processing consisting of brightness and contrast adjustments to emphasize morphological features.

4.2.3 Transmission Electron Microscopy (TEM)

The intermediate phase and final catalysts were further characterized through collaboration with Stephen House in Judith Yangs group on a JEOL JEM 2100F transmission electron microscope. The catalyst morphologies and composition were determined through high–resolution transmission electron microscopy (HRTEM) using an accelerating voltage of 200keV and Energy-dispersive x-ray spectroscopy (EDS) elemental mapping was completed using an Oxford X-MaxN 80T energy-dispersive X-ray spectrometer. The TEM samples were prepared by taking a tiny amount of sample of Ni–Mo catalyst and griding it using a mortar–pestle before dispersing in isopropanol.The solution is sonicated about 5 minutes for better dispersion. After that, two to three drops of the solution are dispersed on a TEM grid and then dried.

4.3 ELECTROCHEMICAL CHARACTERIZATION

Electrodes for the characterization were prepared using Ti foils (Alfa Aesar) that were cut into 5 X 5 mm squares and subsequently cleaned using 5μM alumina and polishing surface. The black Ni–Mo catalyst inks were prepared at known mass concentrations (typically

$\sim$0.02 g/mL due to ease of deposition) and sonicated for 30min prior to deposition. Known quantities of the ink were then deposited on the foil and allowed to dry in air. If a second anneal activation step is required the as prepared Ti foils are put in the borosilicate crucibles and annealed under forming gas at 450*C for 30 minutes in the flow furnace. The gas flow is stopped at the end of 30min and the foils are allowed to cool to room temperature. The foils were then fashioned into electrodes by contacting the Ti foil to a Cu wire using Ag paint. The wire was threaded through a glass capillary and all exposed surfaces except the active electrode area were coated with two–part epoxy. The final electrode will look as illustrated in Fig31

The electrochemical measurements were made using a three electrode electrochemical cell setup shown in Fig32 with an Ag/AgCl reference electrode and Pt counter electrode dipped in freshly prepared 0.1M KOH electrolyte solution saturated with a pure hydrogen gas purge. Solution agitation was provided via fast stirring of a magnetic stir bar. Catalytic activity was evaluated on the basis of mass–specific exchange current densities from cyclic voltammetry (CV) measurements conducted using a Gamry Reference Potentiostat 600. The CV data was collected at scan rates of 10 mV/s and the uncompensated resistance in the cell was accounted for through the Positive Feedback correction tool in the Gamry software. The reversible hydrogen electrode potential (RHE) was determined after each set of experimentation by measuring the open circuit potential of a clean Pt electrode in the same cell setup.

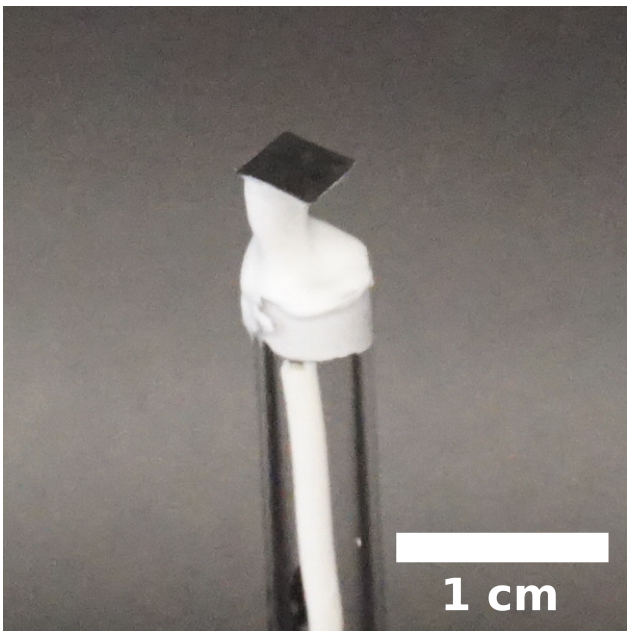

Figure 31: *Photograph of a fully processed electrode coated with Ni–Mo catalyst, taken after electrochemical testing*

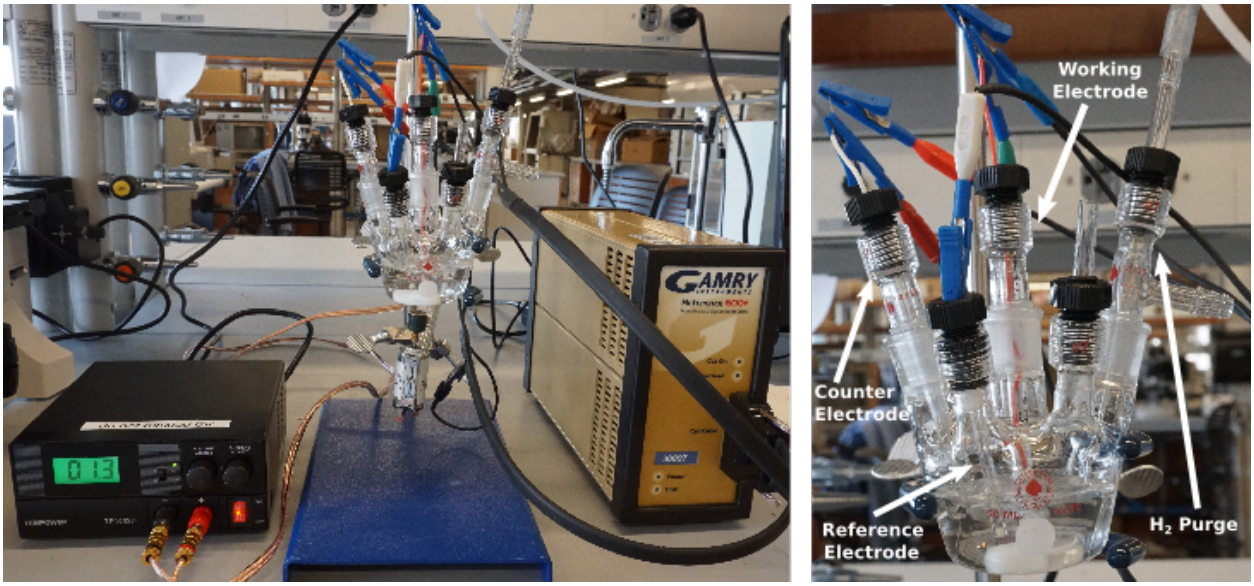

Figure 32: *(left) A typical cell setup along with the potentiostat and rotor that is used to collect cyclic voltammetry data. (right) A typical three electrode setup that was used for this work*

5.0 CONCLUSIONS AND FUTURE WORK

Hydrogen is an important source for producing some of the most critical substances for human sustenance and might possibly become a significant component in our efforts to segue away from conventional fossil fuel sources to renewable energy technology due to its promise as an energy carrier. These factors make for a strong motivation to develop sustainable strategies for its production in the future. Alkaline electrolyzers are one of the many promising H_2 production schemes that can be part of the solution.

The success and widespread implementation of this technology is in part dependent on identifying efficient, stable, and scalable electrocatalysts, one of which could very well be these Ni–Mo catalysts. They have been shown to be highly efficient towards HER and possible to synthesize using highly facile co-precipitation techniques, while only producing environmentally benign byproducts. It has also been demonstrated that the use of carbon additives is effective in dealing with one of the key challenges associated with these systems, the intrinsic low electron conductivity resulting in at least a three-fold activity enhancement over previously synthesized Ni–Mo systems when normalized to catalyst mass.

There is still significant scope for improvements in these catalysts that might help enhance its activity and hopefully allow alkaline electrolysis systems to achieve cost parity with modern day H_2 production schemes including Pt-based PEM electrolyzers. A number of strategies could be suggested in the continued development of these systems. The first of these would be the elucidation of the fundamental mechanistic behavior of Ni-Mo catalysts. This is important for any guided efforts towards enhancing the activity of these systems. In this regard, it is important to understand the significance of crystallographic order between Ni and Mo in these catalysts and the possible relevance of MoO_2 within the bulk. It is also quite possible that the most effective catalysts might be amorphous Ni–Mo composites since

they will allow for the most dispersed presence of adjacent Ni and Mo sites, however, the ability to synthesize such a system is pure conjecture.

It has also been shown that while the co-precipitation technique is useful in synthesizing highly active HER catalysts, these methods offer limited reproducibility. It would be useful to identify the significance of crystalline intermediates in developing active catalysts based on the results from Ch3. Elaboration of the morphology change between the intermediate and final catalyst phases must be an important goal for future work. This would be possible through the use of In-situ TEM analysis of the reduction reaction under the reacting conditions used during the synthesis. This would help ascertain the significance of the precipitation dynamics during catalyst optimization.

In any case, the conceptualization of a continuous precipitation technique for the synthesis $NiMoO_4$ intermediates in this synthetic approach would be useful since it would enable precise control over precipitation conditions while also going a long way in validating the potential of this synthetic method for scale–up. In case, the precipitation dynamics are identified as significant, a continues precipitation technique would also enable precise control over nucleation and particle growth of the intermediate phase. This can be leveraged for inducing a higher degree of nanostructuring in these catalysts in order to improve their active surface area and consequently HER activity.

Another area of further study is the identification of the most effective form of carbon additive in order to enhance the activity of the Ni–Mo system. This work already illustrated the presence of low conductivity in Ni–Mo catalysts as a limitation towards their overall activity. While physical mixtures of Vulcan carbon and Ni–Mo are effective in enhancing the activity to a certain degree, it would be worthwhile to identify the most efficient form of carbon additive. A wide range of graphitic carbon additives can be used as conductivity enhancers of these materials including carbon nanotubes, graphene, graphene oxides etc which might each offer different degrees of dispersion and enhancement in electron transport. Their competence should be evaluated on the basis of the activity scaling possible from their use against the ease of synthesis and device integration associated with their use.

The aforementioned suggestions could be used as bridging steps towards the development of the most active Ni–Mo catalysts. I also believe that demonstration of active catalysts in

functioning electrolyzer set ups are the most effective validation of their potential applicability. The development of a bench top electrolyzer should be a parallel goal within the lab for future work.

Finally, I hope this work bears fruit in providing direction to any researcher coming after me who aims to pursue work on these systems. The goal towards creating a sustainable future is an important one and these systems could possibly make an important component of that future.

BIBLIOGRAPHY

[1] Yergin, D.; Gross, S. Energy for Economic Growth : Energy Vision Update. 2012; https://www.weforum.org/reports?page=29.

[2] Smil Vaclav, *Energy Transitions: Global and National Perspectives*, 2nd ed.; Praeger, 2017.

[3] National Oceanic and Atmospheric Administration, www.ncdc.noaa.gov. 2015; www.ncdc.noaa.gov.

[4] British Petroleum, BP Statistical Review of World Energy. 2017; https://www.bp.com/en/global/corporate/energy-economics/statistical-review-of-world-energy.html.

[5] Solomon, B. D.; Krishna, K. *Energy Policy, Oxford* **2011**, *39*, 7422–7431.

[6] Benck, J. D. Engineering Molybdenum Sulfide electrocatalysts and Silicon Photocathodes for Hydrogen Production via Solar Water Splitting. Ph.D. thesis, Stanford University, 2015.

[7] OSullivan, M.; Overland, I.; Sandalow, D. *The Geopolitics of Renewable Energy*; 2017.

[8] Sørensen, B. *Energy Policy* **1991**, *19*, 8–12.

[9] McKone, J. R. Earth-Abundant Materials for Solar Hydrogen Generation. Ph.D. thesis, California Institute of Technology, 2013.

[10] Lewis, N. S. *MRS Bulletin* **2007**, *32*, 808–820.

[11] United Nations Climate Change Conference, Paris Agreement. 2015; http://unfccc.int/paris_agreement/items/9485.php.

[12] U.S. Energy Information Administration, International Energy Outlook. 2017; https://www.eia.gov/outlooks/ieo/.

[13] Arora, V.; Doman, L. Low and high economic growth cases for China and India. 2017; https://www.eia.gov/outlooks/ieo/lhe.php.

[14] Core Writing Team.,; Pachauri R.K.,; Meyer L.A., IPCC, 2014: Climate Change 2014: Synthesis Report. Contribution of Working Groups I, II and III to the Fifth Assessment Report of the Intergovernmental Panel on Climate Change. 2015; http://www.ipcc.ch/report/ar5/syr/.

[15] U.S. Energy Information Administration, International Energy Outlook. 2013; https://www.eia.gov/outlooks/archive/ieo13/.

[16] Socolow, R.; Pacala, S. *Science* **2004**, *305*, 968–972.

[17] Nakicenovic, N.; Swart, R. IPCC Special Report on Emissions Scenarios : Summary for policymakers. 2000; http://www.ipcc.ch/ipccreports/sres/emission/index.php?idp=0.

[18] Chen, Z. Nanostructuring Molybdenum Disulfide to engineer its surface and bulk properties for solar hydrogen production. Ph.D. thesis, Stanford University, 2012.

[19] Gregory, D. P. *Scientific American* **1973**, *228*, 13–21.

[20] Häussinger, P.; Glatthaar, R.; Rhode, W.; Kick, H.; Benkmann, C.; Weber, J.; Wunschel, H.-J.; Stenke, V.; Leicht, E.; Stenger, H. *Ullmann's Encyclopedia of Industrial Chemistry*; Wiley-VCH Verlag GmbH & Co. KGaA: Weinheim, 2000; Chapter Hydrogen, 6. Uses.

[21] Muradov, N. Z.; Vezirolu, T. N. *International Journal of Hydrogen Energy* **2005**, *30*, 225–237.

[22] Hoffman, P. *The Forever Fuel: The Story of hydrogen*, 1st ed.; Routledge: Boulder, 1981.

[23] Farrauto, R. J. *Hydrocarbon Engineering* **2009**, *14*, 25–30.

[24] National Research Council.,; National Academy of Engineering.,; Division on Engineering and Physical Sciences.,; Board on Energy and Environmental Systems.,; Committee on Alternatives and Strategies for Future Hydrogen Production and Use., *The Hydrogen Economy: Opportunities, Costs, Barriers, and R&D Needs*; The National Academies Press: Washington, DC, 2004.

[25] Balat, M.; Kirtay, E. *Energy Sources, Part A: Recovery, Utilization and Environmental Effects* **2010**, *32*, 863–876.

[26] Kalamaras, C. M.; Efstathiou, A. *Conference Papers in Energy* **2013**, *2013*, Article ID 690627.

[27] Genovese, J.; Harg, K.; Paster, M.; Turner, J. *State-of-the-Art Hydrogen Production Cost Estimate Using Water Electrolysis*; 2009.

[28] Smil, V. *Nature* **1999**, *400*, 415.

[29] Balat, M. *International Journal of Hydrogen Energy* **2008**, *33*, 4013–4029.

[30] de Levie, R. *Journal of Electroanalytical Chemistry* **1999**, *476*, 9293.

[31] Kreuter, W.; Hofmann, H. *International Journal of Hydrogen Energy* **1998**, *23*, 661–666.

[32] Walter, M. G.; Warren, E. L.; McKone, J.; Boettcher, S. W.; Mi, Q.; Santori, E. A.; Lewis, N. S. *Chemical Reviews* **2010**, *110*, 6446–6473.

[33] Bard, A. J.; Faulkner, L. R. *Electrochemistry. I. Faulkner, Larry R*, 6th ed.; Wiley: New York, 1944.

[34] Zou, X.; Zhang, Y. *Chemical Society Reviews* **2015**, *44*, 5148–5180.

[35] Cook, T. R.; Dogutan, D. K.; Reece, S. Y.; Surendranath, Y.; Teets, T. S.; Nocera, D. G. *Chemical Reviews* **2010**, *110*, 6474–6502.

[36] Babic, U.; Suermann, M.; Büchi, F. N.; Gubler, L.; Schmidt, T. J. *Journal of The Electrochemical Society* **2017**, *164*, F387–F399.

[37] Godula-Jopek, A. *Hydrogen Production: By Electrolysis*; Wiley: Singapore, 2015.

[38] da Rosa, A. *Fundamentals of Renewable Energy Processes*, 3rd ed.; Elsevier Inc.: Tokyo, 2009.

[39] Church, S. Del. firm installs fuel cell. 2006.

[40] Grubb, W.; Niedrach, L. *Journal of Electrochemical Society* **1960**, *107*, 132–135.

[41] Mauritz, K. A.; Moore, R. B. *Chemical Reviews* **2004**, *104*, 4535–4586.

[42] Grubb, W. T. Fuel Cell. U.S. Patent 2913511. 1959.

[43] Carmo, M.; Fritz, D. L.; Mergel, J.; Stolten, D. *International Journal of Hydrogen Energy* **2013**, *38*, 4901–4934.

[44] Carmo, M.; Fritz, D.; Maier, W.; Stolten, D. Alkaline Water Electrolysis vs. PEM Water Electrolysis - Exploring their Full Performance. 227th ECS Meeting. Chicago, 2015.

[45] McCrory, C. C. L.; Jung, S.; Peters, J. C.; Jaramillo, T. F. *Journal of the American Chemical Society* **2013**, *135*, 16977–16987.

[46] McCrory, C. C. L.; Jung, S.; Ferrer, I. M.; Chatman, S. M.; Peters, J. C.; Jaramillo, T. F. *Journal of the American Chemical Society* **2015**, *137*, 4347–4357.

[47] Cheng, Y.; Jiang, S. P. *Progress in Natural Science-Materials International* **2015**,

[48] Greeley, J.; Nørskov, J. K.; Kibler, L. A.; El-Aziz, A. M.; Kolb, D. M. *ChemPhysChem* **2006**, *7*, 1032–1035.

[49] Yan, Y.; Xia, B. Y.; Zhao, B.; Wang, X. *Journal of Materials Chemistry* **2016**, *4*, 17587–17603.

[50] Vesborg, P. C.; Seger, B.; Chorkendorff, I. *Journal of Physical Chemistry Letters* **2015**, *6*, 951–957.

[51] Santos, D. M. F.; Sequeira, C. A. C.; Macciò, D.; Saccone, A.; Figueiredo, J. L. *International Journal of Hydrogen Energy* **2013**, *38*, 3137–3145.

[52] Lu, X.; Zhao, C. *Nature Communications* **2015**, *6*, 6616.

[53] Merrill, M.; Dougherty, R. *Journal of Physical Chemistry C* **2008**, *112*, 3655–3666.

[54] Laursen, A. B.; Kegnæs, S.; Dahl, S.; Chorkendorff, I. *Energy & Environmental Science* **2012**, *5*, 5577–5591.

[55] Kibler, L. A. *ChemPhysChem* **2006**, *7*, 985–991.

[56] Rothenberg, G. *Catalysis: Concepts and Green Applications*; WileyVCH: Weinheim, 2008.

[57] Laursen, A. B.; Varela, A. S.; Dionigi, F.; Fanchiu, H.; Miller, C.; Trinhammer, O. L.; Rossmeisl, J.; Dahl, S. *Journal of Chemical Education* **2012**, *89*, 1595–1599.

[58] Miles, M. H. *Journal of Electroanalytical Chemistry* **1975**, *60*, 89–96.

[59] Trasatti, S. *Journal of Electroanalytical Chemistry* **1972**, *39*, 163–184.

[60] Walter, M. G.; Warren, E. L.; McKone, J.; Boettcher, S. W.; Mi, Q.; Santori, E. A.; Lewis, N. S. *Chemical Reviews* **2010**, *110*, 6446–6473.

[61] Jaramillo, T. F.; Jørgensen, K. P.; Bonde, J.; Nielsen, J. H.; Horch, S.; Chorkendorff, I. *Science* **2007**, *317*, 100–102.

[62] Greeley, J.; Jaramillo, T. F.; Bonde, J.; Chorkendorff, I.; Nørskov, J. K. *Nature Materials* **2006**, *5*, 909–913.

[63] Hinnemann, B.; Moses, P. G.; Bonde, J.; Jørgensen, K. P.; Nielsen, J. H.; Horch, S.; Chorkendorff, I.; Nørskov, J. K. *Journal of the American Chemical Society* **2005**, *127*, 5308–5309.

[64] Tang, M. H.; Hahn, C.; Klobuchar, A. J.; Ng, J. W. D.; Wellendorff, J.; Bligaard, T.; Jaramillo, T. F. *Physical Chemistry Chemical Physics* **2014**, *16*, 19250–19257.

[65] Durst, J.; Siebel, A.; Simon, C.; Hasché, F.; Herranz, J.; Gasteiger, H. A. *Energy & Environmental Science* **2014**, *7*, 2255–2260.

[66] Mahmood, N.; Yao, Y.; Zhang, J.-W.; Pan, L.; Zhang, X.; Zou, J.-J. *Advanced Science* **2018**, *5*, 1700464.

[67] Cheng, N.; Stambula, S.; Wang, D.; Banis, M. N.; Liu, J.; Riese, A.; Xiao, B.; Li, R.; Sham, T. K.; Liu, L. M.; Botton, G. A.; Sun, X. *Nature Communications* **2016**, *7*, 16368.

[68] Sun, S. et al. *Scientific Reports* **2013**, *3*, 1775.

[69] Bates, M. K.; Jia, Q.; Ramaswamy, N.; Allen, R. J.; Mukerjee, S. *Journal of Physical Chemistry C* **2015**, *119*, 5467–5477.

[70] McKone, J. R.; Sadtler, B. F.; Werlang, C. A.; Lewis, N. S.; Gray, H. B. *ACS Catalysis* **2013**, *3*, 166–169.

[71] Zhang, J.; Wang, T.; Liu, P.; Liao, Z.; Liu, S.; Zhuang, X.; Chen, M.; Zschech, E.; Feng, X. *Nature Communications* **2017**, 15437.

[72] Popczun, E. J.; McKone, J. R.; Read, C. G.; Biacchi, A. J.; Wiltrout, A. M.; Lewis, N. S.; Schaak, R. E. *Journal of the American Chemical Society* **2013**, *135*, 9267–9270.

[73] Brown, D. E.; Mahmood, M. N.; Turner, A. K.; Hall, S. M.; Fogarty, P. O. *International Journal of Hydrogen Energy* **1982**, *7*, 405–410.

[74] Brown, D. E.; Mahmood, M. N.; Man, M. C.; Turner, A. K. *Electrochimica Acta* **1984**, *29*, 1551–1556.

[75] Raj, I. A.; Vasu, K. I. *Journal of Applied Electrochemistry* **1992**, *22*, 471–477.

[76] Arul Raj, I.; Venkatesan, V. K. *International Journal of Hydrogen Energy* **1988**, *13*, 215–223.

[77] Stachurski, J. Z. O.; Pouli, D.; Ripa, J. A.; Pokrzyk, G. F. Low overvoltage hydrogen cathodes. U.S. Patent 4354915A. 1982.

[78] Conway, B. E.; Angerstein-Kozlowska, H.; Sattar, M. A.; Tilak, B. V. *Journal of The Electrochemical Society* **1983**, *130*, 1825–1836.

[79] Conway, B. E.; Tilak, B. V. *Electrochimica Acta* **2002**, *47*, 3571–3594.

[80] Raj, I. A. *Journal of Materials Science* **1993**, *28*, 4375–4382.

[81] Raj, I. A. *International Journal of Hydrogen Energy* **1992**, *17*, 413–421.

[82] Conway, B. E.; Bai, L. *International Journal of Hydrogen Energy* **1986**, *11*, 533–540.

[83] Brown, D. E.; Mahmood, M. N. Method of preparing active electrodes. U.S. Patent 4358475. 1982.

[84] Akhtar, N.; Decent, S. P.; Kendall, K.; Li, Y. S.; Zhao, T. S.; Mehta, V.; Cooper, J. S. *International Journal of Hydrogen Energy* **2003**, *114*, 32–53.

[85] Litster, S.; McLean, G. *Journal of Power Sources* **2004**, *130*, 61–76.

[86] Csernica, P. M.; McKone, J. R.; Mulzer, C. R.; Dichtel, W. R.; Abruña, H. D.; DiSalvo, F. J. *ACS Catalysis* **2017**, *7*, 3375–3383.

[87] Fan, C. *Journal of The Electrochemical Society* **1994**, *141*, 382–387.

[88] Navarro-Flores, E.; Chong, Z.; Omanovic, S. *Journal of Molecular Catalysis A: Chemical* **2005**, *226*, 179–197.

[89] Jakšić, J. M.; Vojnović, M. V.; Krstajić, N. V. *Electrochimica Acta* **2000**, *45*, 4151–4158.

[90] Highfield, J. G.; Claude, E.; Oguro, K. *Electrochimica Acta* **1999**, *44*, 2805–2814.

[91] Levin, D.; Soled, S. L.; Ying, J. Y. *Inorganic Chemistry* **1996**, *35*, 4191–4197.

[92] Schmitt, P.; Brem, N.; Schunk, S.; Feldmann, C. *Advanced Functional Materials* **2011**, *21*, 3001–3197.

[93] Killeffer, A., D. H.; Linz *Molybdenum compounds, their chemistry and technology*, 1st ed.; Interscience Publishers: New York, 1952.

[94] Dong, H.; Chen, Y.-C.; Feldmann, C. *Green chemistry* **2015**, *17*, 4107–4132.

[95] Pezerat, H. *Comptes rendus hebdomadaires des séances de lAcadémie des sciences. Série C, Sciences chimiques* **1965**, *261*, 5490–5493.

[96] Pezerat, H.; Mantin, I.; Kovacevic, S. *Comptes rendus hebdomadaires des séances de lAcadémie des sciences. Série C, Sciences chimiques* **1966**, *262*, 95–98.

[97] Madeira, L. M.; Portela, M. F.; Mazzocchia, C. *Catalysis Reviews - Science and Engineering* **2004**, *46*, 53–110.

[98] Mazzocchia, C.; Tempesti, E.; Aboumrad, C. Catalyst for oxidative dehydrogenation of propane. U.S. Patent 5086032A. 1992.

[99] Cai, D.; Wang, D.; Liu, B.; Wang, Y.; Liu, Y.; Wang, L.; Li, H.; Huang, H.; Li, Q.; Wang, T. *ACS Applied Materials & Interfaces* **2013**, *5*, 12905–12910.

[100] Kianpour, G.; Soofivand, F.; Badiei, M.; Salavati-Niasari, M.; Hamadanian, M. *Journal of Materials Science: Materials in Electronics* **2016**, *27*, 10244–10251.

[101] Gennero de Chialvo, M. R.; Chialvo, A. C. *Journal of Electroanalytical Chemistry* **1998**, *448*, 87–93.

[102] Saravanakumar, B.; Ramachandran, S. P.; Ravi, G.; Ganesh, V.; Sakunthala, A.; Yuvakkumar, R. *Materials Letters* **2017**, *209*, 1–4.

[103] Li, J.; Yan, M.; Zhou, X.; Huang, Z.-Q.; Xia, Z.; Chang, C.-R.; Ma, Y.; Qu, Y. *Advanced Functional Materials* **2016**, *26*, 6785–6796.

[104] Duan, J.; Chen, S.; Zhao, C. *Nature Communications* **2017**, 15341.

[105] Viswanathan, V.; Pickrahn, K. L.; Luntz, A. C.; Bent, S. F.; Nørskov, J. K. *Nano Letters* **2014**, *14*, 5853–5857.

[106] Zhu, C.; Fu, S.; Xu, B. Z.; Song, J.; Shi, Q.; Engelhard, M. H.; Li, X.; Beckman, S. P.; Sun, J.; Du, D.; Lin, Y. *Small* **2017**, *13*, 1700796.

[107] Gong, M.; Wang, D. Y.; Chen, C. C.; Hwang, B. J.; Dai, H. *Nano Research* **2016**, *9*, 28–46.

[108] Wang, J.; Qiu, T.; Chen, X.; Lu, Y.; Yang, W. *Journal of Power Sources* **2015**, *293*, 178–186.

[109] Xiao, J.; Zhao, C.; Hu, C.; Xi, J.; Wang, S. *Journal of Power Sources* **2017**, *348*, 183–192.

[110] Zeng, F.; Broicher, C.; Palkovits, S.; Simeonov, K.; Palkovits, R. *Catalysis Science and Technology* **2018**, *8*, 367–375.

[111] Cao, P.; Peng, J.; Liu, S.; Cui, Y.; Hu, Y.; Chen, B.; Li, J.; Zhai, M. *Scientific Reports* **2017**, *7*, 16048.

[112] Andrushkevich, M. M.; Buyanov, R. A.; Sitnikov, V. G.; Itenberg, I. S.; Khramova, G. A. *Kinetics and Catalysis* **1973**, *14*, 464.

[113] Okamoto, H. .; Schlesinger, M. E.; Mueller, E. M. *ASM Handbook; Volume 03 - Alloy Phase Diagrams*; ASM International: Materials Park, Ohio, 2016.

[114] Danilovic, N.; Subbaraman, R.; Strmcnik, D.; Chang, K. C.; Paulikas, A. P.; Stamenkovic, V. R.; Markovic, N. M. *Angewandte Chemie - International Edition* **2012**, *51*, 12495–12498.

[115] Subbaraman, R.; Tripkovic, D.; Strmcnik, D.; Chang, K. C.; Uchimura, M.; Paulikas, A. P.; Stamenkovic, V.; Markovic, N. M. *Science* **2011**, *334*, 1256–1260.

[116] Sheng, C.; Gasteiger, H. A.; Shao-Horn, Y.; Sheng, W. *Journal of the Electrochemical Society* **2010**, *157*, B1529–B1536.

[117] Zheng, Y.; Jiao, Y.; Zhu, Y.; Li, L. H.; Han, Y.; Chen, Y.; Jaroniec, M.; Qiao, S. Z. *Journal of the American Chemical Society* **2016**, *138*, 16174–16181.

[118] Ertl, G.; Knozinger, H.; Weitkamp, J. *Preparation of Solid Catalysts*; Wiley-VCH: Weinheim, Chichester, 1999.

[119] Haber, J.; Block, J. H.; Delmon, B. *Manual of methods and procedures for catalyst characterization*; 1995; pp 1257–1306.

[120] Joh, H. I.; Seo, S. J.; Kim, H. T.; Moon, S. H. *Korean Journal of Chemical Engineering* **2010**, *27*, 45–48.

[121] Málek, J.; Watanabe, A.; Mitsuhashi, T. *Thermochimica Acta* **1996**, *282*, 131–142.